IEEE TRANSACTIONS ON POWER ELECTRONICS, VOL. 40, NO. 9, SEPTEMBER 2025

Multifrequency Model of Dual Active Bridge Resonant Converters With Phase-Shift Control

Xin Li, *Member, IEEE*, Pengfei Yao, Jianing Li, Peili Yuan, Jiangfeng Wang, *Member, IEEE*,
Wu Chen, *Senior Member, IEEE*, and Yi Tang, *Senior Member, IEEE*

***Abstract*—The dual-active-bridge (DAB) resonant converters are a cluster of efficient bidirectional dc-dc converters. It is commonly a challenge to obtain the analytic expressions of the control-to-output transfer functions especially in multi-element resonant converters. In this article, the multifrequency modeling technique is adopted to derive the general small-signal model for DAB resonant converters with various resonant tanks. The analytic expression of phase-shift-angle-to-output-voltage transfer function as well as the general control block diagram of DAB resonant converter is obtained. It is interesting to see that the models are different depending on primary side phase shift or secondary side phase shift. To have a clear picture of the differences, order reductions of the models are conducted with the example of the DAB series resonant converter. Finally, the prototype of the DAB series resonant converter is built in the lab, and the phase-shift-angle-to-output-voltage transfer function is measured, which successfully verifies the validity of the proposed model.**

***Index Terms*—Dual active bridge (DAB) resonant converter, multifrequency model, primary side phase shift or secondary side phase shift, small-signal modeling.**

I. INTRODUCTION

THE dual-active-bridge (DAB) resonant converter, as shown in Fig. 1, inherits both the advantages of DAB converters and the unidirectional resonant converters, such as easy achievement of soft switching, flexibility of power control, wide input voltage range, low EMI issue, making them favored bidirectional converters in medium and high-power occasions nowadays [1], [2], [3], [4].

Small-signal modeling is the foundation for dynamic analysis of converters, with which, it is possible to obtain a precise control loop design procedure, thus systematically improving the stability and dynamic performance of the converter. In [4], a discrete-time small signal model of DAB series resonant converter (DABSRC) with both frequency and PWM control is established, and the relevant symbol transfer function is derived. It shows when the time constant of the load is much higher than the switching frequency and for pulsewidth regulation, the converter is similar in properties to the stationary linear element of the third order. In [5], a discrete model for single phase-shift control DABSRC is also proposed to qualitatively discuss the impact of dead zone on the resonance peak of the model. Despite being accurate, discrete-time modeling rarely yields closed-form transfer functions that can be expressed in terms of circuit parameters, owing to the computational complexity associated with the matrix exponential function. Consequently, these functions cannot be evaluated symbolically in a manner conducive to design-oriented analysis.

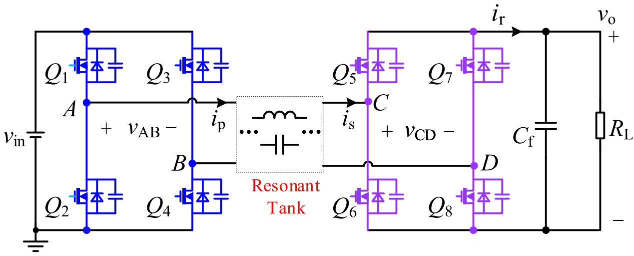

Fig. 1. General topology of a DAB resonant converter.

To simplify the modeling process, a method that mixes the Fourier and the state-space averaging was developed in [6] to investigate the transient response of the discontinuous mode DABSRC. This method facilitates the modeling of converters with multiple operating modes within one cycle and in one of them the current is zero. However, as the authors admitted, the accuracy is worse than the traditional state-space averaging method. In [7] and [8], modeling under fault tolerance operation is discussed, where the resonant network of DABSRC is approximated as a single inductor as per the principle of storing the same total energy. This leads to a second-order small signal model of DABSRC, which is essentially a periodic averaging model that is only applicable for analyzing low frequency oscillation mechanisms.

It is worth mentioning that the above modeling methods are basically limited to modeling simple converters. Some modeling methods that combine time and frequency analysis have been

---

Received 14 January 2025; revised 4 April 2025; accepted 4 May 2025. Date of publication 13 May 2025; date of current version 30 June 2025. This work was supported in part by the National Science Foundation of China under Grant 52307196, in part by the Natural Science Foundation of Jiangsu Province under Grant BK20230850, and in part by the Jiangsu Provincial Key Laboratory of Smart Grid Technology and Equipment under Grant 4216002201. Recommended for publication by Associate Editor L. Corradini. *(Corresponding author: Wu Chen.)*

Xin Li, Pengfei Yao, Jianing Li, Peili Yuan, Jiangfeng Wang, and Wu Chen are with the School of Electrical Engineering, Southeast University, Nanjing 210096, China (e-mail: li-xin@seu.edu.cn; yao-pengfei@seu.edu.cn; 220243073@seu.edu.cn; 220243087@seu.edu.cn; jfwang@seu.edu.cn; chenwu@seu.edu.cn).

Yi Tang is with the School of Electrical and Electronic Engineering, Nanyang Technological University, Singapore 639798 (e-mail: yitang@ntu.edu.sg).

Color versions of one or more figures in this article are available at https://doi.org/10.1109/TPEL.2025.3569745.

Digital Object Identifier 10.1109/TPEL.2025.3569745

broadly used in modeling various DAB resonant converters owing to its relatively simple and systematic derivation. These methods mainly include the generalized state space averaging (GSSA) method, the extended describing function (EDF) method, and the Laplace phasor transform (LPT). In [9] and [10], the EDF and GSSA methods are, respectively, employed to obtain the DABSRC with single phase-shift control. Seltzer et al. [11] utilized the DPT method to construct the small signal phasor modeling of DABSRC with multiangle phase shift modulation, and transfer functions from random angle to the output are deduced. Subsequently, a gain-scheduled approach for DABSRC was demonstrated on the basis of the models in [12], providing optimal performance at different conversion ratios and power levels. In [13], a GSSA-based model of a dual active half-bridge resonant converter with *LC* filtering circuit is established. In [14] and [15], the small-signal models of *CLLC* resonant converter are obtained by the EDF and DPT methods, respectively. Malan et al. [16] did a similar work to DAB *CLLC* converter with [14]. Although it is claimed the dq modeling method, but essentially also fallen in the scope of the aforementioned three methods. Li et al. [17] extended it to bidirectional *CLLLC* converter. Scandola et al. [18] adopted the DPT method to model and analyze the digital controlled dual active half bridge resonant converter. This study extended known results for uniformly sampled pulsewidth and phase shift modulators, and illustrated the effects of sampling delays on the modulator output dynamics.

Although EDF, DPT, and GSSA methods provide a clear and universal modeling process for all kinds of resonant converters, it should be pointed out that to obtain the explicit transfer functions, all the state variables in the resonant tank are decomposed into real and imaginary parts, forming a high-order matrix. If the DAB resonant converter has n resonant elements, the order of the matrix will be $2n+1$. Therefore, it will be very hard to obtain explicit transfer functions of multielement DAB resonant converter in this way.

In addition, as shown in Fig. 2, DAB resonant converter with phase-shift modulation has two different implementation methods. In Fig. 2(a), the secondary bridge is fixed while the primary side bridge is regulated. In Fig. 2(b), the bridge on primary side bridge is fixed while that on the secondary bridge is regulated. According to the authors' review, most of the existing literature focuses on the modeling of Fig. 2(a), which gives the illusion that the small-signal models of the two SPS implementation methods are the same. However, in this article, it is interesting to find that the two implementation methods lead to two distinct models. In other words, there exists two possible models for any DAB resonant converter with single-phase-control, which has not been explained.

To address these issues, a simpler and more accurate modeling method is expected. The multifrequency modeling method was developed in [19] to investigate the sideband effect of the PWM converters. In 2021, it was successfully applied to modeling resonant converter by the authors [20]. The core idea of multifrequency modeling is using the ratio of the complex Fourier coefficients of different frequencies to represent the transfer function between the two frequencies. Based on this, the resonant tank can be regarded as a whole during the modeling, thus avoiding the $2n+1$ matrices, and making it possible to obtain analytic expressions of the transfer functions. However, the state-of-art research is limited to unidirectional resonant converters with simple diode rectification. With the considerations above, this article intends to have a thorough modeling of the phase-shift DAB resonant converters using the multifrequency modeling method, and distinguishes the two implementation methods of phase shift mathematically.

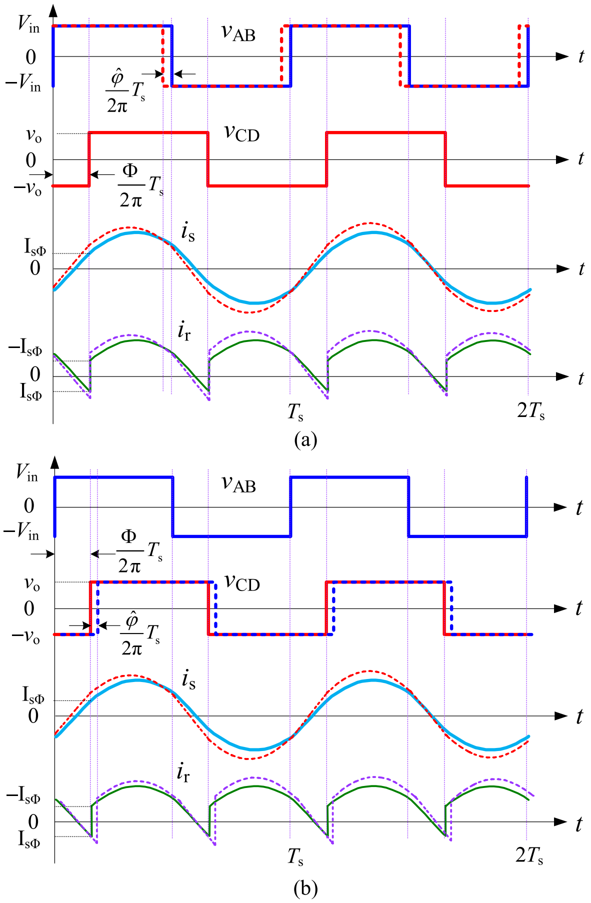

(a)

(b)

Fig. 2. Key waveforms of a DAB resonant converter with different phase shift schemes. (a) Primary-side regulation. (b) Secondary-side regulation.

The rest of this article is organized as follows. Sections II and III give the generalized modeling process of DAB resonant converter with primary side regulation and secondary side regulation, respectively. Section IV takes the DABSRC as an example to have the order of the models reduced to obtain the analytic expressions, based on which, the differences between the primary side regulation and secondary side regulation are discussed mathematically. Section V provides the experimental result to validate the analysis. Finally, Section VI concludes this article.

II. MODELING OF DAB RESONANT CONVERTER WITH PRIMARY SIDE REGULATION

For the DAB resonant converter in Fig. 1, Q_1–Q_4 are the switches on the primary side, Q_5–Q_8 are the switches on the

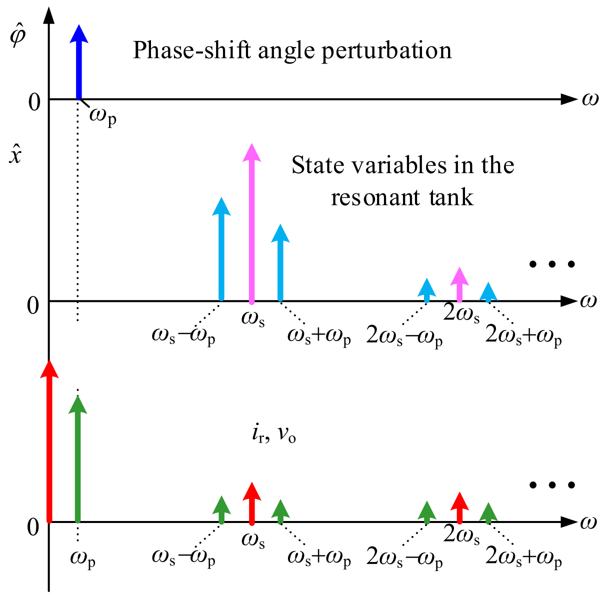

Fig. 3. Spectra of the current (voltage) waveforms of state variable x of a converter when the modulation signal of the phase-shift angle is perturbed with ω_p component.

secondary side, C_f is the output filter capacitor with the equivalent series resistor R_c. R_{Ld} is the load resistor. v_{in} is the input voltage, v_{AB} and i_p are the output voltage and output current of the bridge on the primary side, v_{CD} and i_s are the input voltage and input current of the bridge on the secondary side, i_r is the rectified current, v_{cf} is the voltage across C_f, v_o is the output voltage. The phase shift angle φ presents the phase that v_{AB} is in advanced of v_{CD}, which ranges from -π to π.

As depicted in Fig. 3, when the phase-shift angle φ undergoes a small-signal perturbation at the frequency ω_p (where $\omega_p << \omega_s$), signals throughout the converter produce components of $n\omega_s \pm \omega_p$ (with $n \neq 0$), referred to as sideband components. Given that the switching frequency is closely tuned to the resonant frequency, the $\omega_s \pm \omega_p$ components become dominant within the resonant tank. Due to the low-pass filter characteristics, the ω_p component predominantly influences v_o and i_r. Therefore, it is essential to account for the $\omega_s \pm \omega_p$ components in the resonant tank and the ω_p component in the output port waveforms.

In this section, the multifrequency model of the DAB resonant converter with primary-side regulation will be derived. The key signals under phase-shift angle perturbation, including v_{AB}, i_s, i_r, v_o, and v_{CD}, will be derived separately and ultimately form a complete block diagram.

A. *Small-Signal Expression of* v_{AB}

As shown in Fig. 2(a), when the phase-shift angle φ is perturbed with a small-signal component $\hat{\varphi}(t)$, v_{AB} will vary accordingly, the expression of v_{AB} in a switching cycle is as follows:

$$v_{AB}(t) = \begin{cases} V_{in} & \text{if } -\frac{\hat{\varphi}}{2\pi}T_s \le t < \frac{1}{2}T_s - \frac{\hat{\varphi}}{2\pi}T_s \\ -V_{in} & \text{if } \frac{1}{2}T_s - \frac{\hat{\varphi}}{2\pi}T_s \le t \le T_s - \frac{\hat{\varphi}}{2\pi}T_s. \end{cases} \quad (1)$$

Obviously, v_{AB} is a square wave comprising numerous harmonics. Given that the switching frequency is typically tuned close to the resonant frequency, only the fundamental harmonic component of v_{AB} is effective in generating the resonant current. Therefore, v_{AB} can be approximated using the fundamental harmonic analysis (FHA) method. By performing Fourier transform on (1), the fundamental harmonic component of v_{AB} can be expressed as follows:

$$v_{AB}(t) \approx \frac{4}{\pi} V_{in} \sin\left[\omega_s t + \hat{\varphi}(t)\right]. \quad (2)$$

Linearizing (2) around the equilibrium point leads to the following equation, the small-signal expression of v_{AB}, denoted as $\hat{v}_{AB}(t)$ is as follows:

$$\hat{v}_{AB}(t) \approx \frac{\partial v_{AB}(t)}{\partial \varphi}\hat{\varphi}(t) = \frac{4}{\pi} V_{in} \hat{\varphi}(t) \cos(\omega_s t). \quad (3)$$

Assuming the perturbation frequency is ω_p, $\hat{\varphi}(t)$ can be expressed as follows:

$$\hat{\varphi}(t) = \hat{\Phi}\cos(\omega_p t + \theta_\varphi) = \frac{\hat{\Phi}}{2} e^{j\theta_\varphi} e^{j\omega_p t} + \frac{\hat{\Phi}}{2} e^{-j\theta_\varphi} e^{-j\omega_p t} \quad (4)$$

where $\hat{\Phi}$ and θ_φ are the amplitude and initial phase of $\hat{\varphi}(t)$, respectively.

Moreover, according to Euler's formula, we have

$$\cos(\omega_s t) = \frac{1}{2} e^{j\omega_s t} + \frac{1}{2} e^{-j\omega_s t}. \quad (5)$$

Substituting (4) and (5) into (3), the expression of $\hat{v}_{AB}(t)$ in complex frequency domain is as follows:

$$\begin{aligned} \hat{v}_{AB}(t) &= \frac{4}{\pi} V_{in} \hat{\varphi} \cos(\omega_s t) \\ &= \frac{4}{\pi} V_{in} \left(\frac{\hat{\Phi}}{2} e^{j\theta_\varphi} e^{j\omega_p t} + \frac{\hat{\Phi}}{2} e^{-j\theta_\varphi} e^{-j\omega_p t}\right)\left(\frac{1}{2} e^{j\omega_s t} + \frac{1}{2} e^{-j\omega_s t}\right) \\ &= \frac{V_{in}}{\pi} \hat{\Phi} \left(e^{j\theta_\varphi} e^{j\omega_p t} + e^{-j\theta_\varphi} e^{-j\omega_p t}\right)\left(e^{j\omega_s t} + e^{-j\omega_s t}\right) \\ &= \frac{V_{in}}{\pi} \hat{\Phi} e^{j\theta_\varphi} e^{j(\omega_p - \omega_s)t} + \frac{V_{in}}{\pi} \hat{\Phi} e^{-j\theta_\varphi} e^{j(\omega_s - \omega_p)t} \\ &\quad + \frac{V_{in}}{\pi} \hat{\Phi} e^{j\theta_\varphi} e^{j(\omega_p + \omega_s)t} + \frac{V_{in}}{\pi} \hat{\Phi} e^{-j\theta_\varphi} e^{-j(\omega_s + \omega_p)t}. \end{aligned} \quad (6)$$

Note that there exist $\omega_p \pm \omega_s$ components and $\omega_s \pm \omega_p$ components in (6), which are conjugate. As a result, only $\omega_p \pm \omega_s$ components need to be considered for convenience. According to (6), the Fourier coefficients of the $\omega_p + n\omega_s$ component in $\hat{v}_{AB}(t)$ is expressed as follows:

$$v_{AB}[j(\omega_p - \omega_s)] = \frac{V_{in}}{\pi} \hat{\Phi} e^{j\theta_\varphi} \quad (7)$$

$$v_{AB}[j(\omega_p + \omega_s)] = \frac{V_{in}}{\pi} \hat{\Phi} e^{j\theta_\varphi}. \quad (8)$$

Considering the Fourier coefficient of the ω_p component in $\hat{\varphi}(t)$ is as follows:

$$\varphi(j\omega_p) = \frac{\hat{\Phi}}{2} e^{j\theta_\varphi}. \quad (9)$$

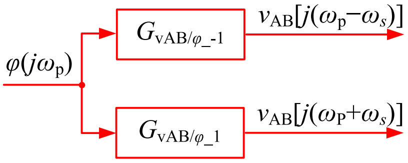

Fig. 4. Control block diagram of the multifrequency model from φ to v_{AB} under primary side regulation.

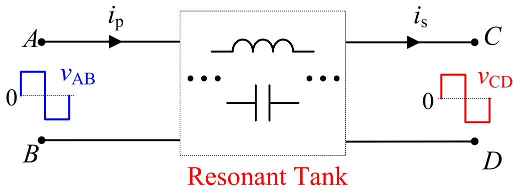

Fig. 5. Uniformly two-port network representation of the resonant tank under primary-side regulation.

Therefore, the transfer function from $\varphi(j\omega_{\mathrm{p}})$ to v_{AB} $[j(\omega_{\mathrm{p}} + n\omega_{\mathrm{s}})]$, defined as $G_{\mathrm{vAB}\ /\varphi\_n}$, is obtained as follows for $n = \pm 1$:

$$G_{\mathrm{vAB}/\varphi\_-1} = \frac{v_{\mathrm{AB}}[j(\omega_{\mathrm{p}} - \omega_{\mathrm{s}})]}{\varphi\left(j\omega_{\mathrm{p}}\right)} = \frac{2V_{\mathrm{in}}}{\pi}. \tag{10}$$

$$G_{\mathrm{vAB}/\varphi\_1} = \frac{v_{\mathrm{AB}}[j(\omega_{\mathrm{p}}+\omega_{\mathrm{s}})]}{\varphi\left(j\omega_{\mathrm{p}}\right)} = \frac{2V_{\mathrm{in}}}{\pi}. \tag{11}$$

The control block diagram of the model from φ to v_{AB} under primary-side regulation is depicted in Fig. 4.

B. Small-Signal Expression of I_s

For the DAB resonant converter in Fig. 1, the resonant tank can be uniformly depicted with the linear time-invariant two-port network, as shown in Fig. 5. The two port voltages are v_{AB} and v_{CD}. The expression of the input current of the rectifier, i_{s}, can be represented in frequency domain as follows:

$$i_{\mathrm{s}}(s) = \frac{v_{\mathrm{AB}}(s)}{Z_{\mathrm{AB}}(s)} - \frac{v_{\mathrm{CD}}(s)}{Z_{\mathrm{CD}}(s)} \tag{12}$$

where $Z_{\mathrm{AB}}(s)$ and $Z_{\mathrm{CD}}(s)$ are the impedances subject to the topology selected. When φ is perturbed, both v_{AB} and v_{CD} contain the $\omega_{\mathrm{p}} \pm \omega_{\mathrm{s}}$ components. As a result, we have

$$i_{\mathrm{s}}[j(\omega_{\mathrm{p}} - \omega_{\mathrm{s}})] = \frac{v_{\mathrm{AB}}[j(\omega_{\mathrm{p}} - \omega_{\mathrm{s}})]}{Z_{\mathrm{AB}}[j(\omega_{\mathrm{p}} - \omega_{\mathrm{s}})]} - \frac{v_{\mathrm{CD}}[j(\omega_{\mathrm{p}} - \omega_{\mathrm{s}})]}{Z_{\mathrm{CD}}[j(\omega_{\mathrm{p}} - \omega_{\mathrm{s}})]}. \tag{13}$$

Equation (13) is the model of the resonant tank that applies to various DAB resonant topologies under primary-side regulation. The corresponding control block diagram is shown in Fig. 6. Please note that there is no interaction between $\omega_{\mathrm{p}} + \omega_{\mathrm{s}}$ component and $\omega_{\mathrm{p}} - \omega_{\mathrm{s}}$ component since it is a linear time-invariant network.

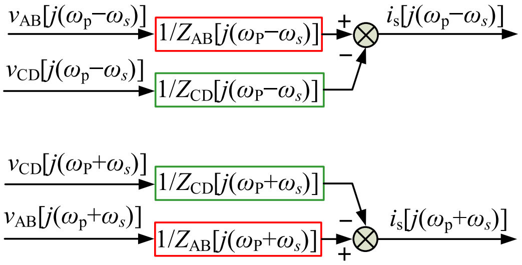

Fig. 6. General multifrequency small-signal model for resonant tank under primary-side regulation.

C. Small-Signal Expression of I_r and V_o

According to the previous deduction, i_{s} contains $\omega_{\mathrm{p}} \pm \omega_{\mathrm{s}}$ components, which can be expressed as follows:

$$\hat{i}_{\mathrm{s}}(t) = \sum_{n=-1,+1} \hat{I}_{\mathrm{speak}n} \cos\left(\omega_{\mathrm{p}}t + n\omega_{\mathrm{s}}t + \theta_{\mathrm{isN}}\right) \tag{14}$$

where the values of n are ± 1.

Besides, the steady-state fundamental harmonic component is represented as follows:

$$I_{\mathrm{s}}(t) = I_{\mathrm{speak}} \cos(\omega_{\mathrm{s}}t + \Theta_{\mathrm{Is}}). \tag{15}$$

Combining (14) and (15) together, i_{s} is expressed as follows:

$$\begin{aligned} i_{\mathrm{s}}(t) &= I_{\mathrm{speak}} \cos(\omega_{\mathrm{s}}t + \Theta_{\mathrm{Is}}) \\ &\quad + \sum_{n=-1,+1} \hat{I}_{\mathrm{speak}n} \cos\left(\omega_{\mathrm{p}}t + n\omega_{\mathrm{s}}t + \theta_{\mathrm{isN}}\right). \end{aligned} \tag{16}$$

The expression of i_{r} is as follows:

$$i_{\mathrm{r}}(t) = \begin{cases} i_{\mathrm{s}}(t) & \text{if } \frac{\Phi}{2\pi}T_{\mathrm{s}} \le t < \frac{\Phi}{2\pi}T_{\mathrm{s}} + \frac{1}{2}T_{\mathrm{s}} \\ -i_{\mathrm{s}}(t) & \text{if } \frac{\Phi}{2\pi}T_{\mathrm{s}} + \frac{1}{2}T_{\mathrm{s}} \le t < \frac{\Phi}{2\pi}T_{\mathrm{s}} + T_{\mathrm{s}} \end{cases}. \tag{17}$$

The ω_{p} component in i_{r} will be derived here. To facilitate the derivation, it is assumed that there exists a common frequency ω_0, satisfying

$$\omega_{\mathrm{p}} = M\omega_0, \omega_{\mathrm{s}} = N\omega_0. \tag{18}$$

Thus, the periods of the three frequencies meet

$$T_0 = MT_{\mathrm{p}} = NT_{\mathrm{s}}. \tag{19}$$

Here, ω_0 is regarded as the "virtual" fundamental frequency, hence, the frequency $\omega_{\mathrm{p}}+n\omega_{\mathrm{s}}$ ($n = \pm 1$) can also be expressed as $(M + nN)\omega_0$. Based on (16)–(19), the Fourier coefficient of the ω_{p} component in i_{r} can be obtained as follows:

$$\begin{aligned} i_{\mathrm{r}}\left(j\omega_{\mathrm{p}}\right) &= i_{\mathrm{r}}\left(jM\omega_0\right) \\ &= \frac{1}{T_0} \sum_{l=0}^{N-1} \int_{lT_{\mathrm{s}}+\frac{\Phi}{2\pi}T_{\mathrm{s}}}^{lT_{\mathrm{s}}+\frac{\Phi}{2\pi}T_{\mathrm{s}}+\frac{1}{2}T_{\mathrm{s}}} \hat{I}_{\mathrm{speak}n} \cos[(M + nN)\omega_0 t \\ &\quad + \theta_{\mathrm{is}n}]e^{-jM\omega_0 t}dt \\ &\quad - \frac{1}{T_0} \sum_{l=0}^{N-1} \int_{lT_{\mathrm{s}}+\frac{\Phi}{2\pi}T_{\mathrm{s}}+\frac{1}{2}T_{\mathrm{s}}}^{lT_{\mathrm{s}}+\frac{\Phi}{2\pi}T_{\mathrm{s}}+T_{\mathrm{s}}} \hat{I}_{\mathrm{speak}n} \cos[(M + nN)\omega_0 t \\ &\quad + \theta_{\mathrm{is}n}]e^{-jM\omega_0 t}dt. \end{aligned} \tag{20}$$

After extensive derivations, it is obtained that

$$\begin{aligned} i_{\mathrm{r}}\left(j\omega_{\mathrm{p}}\right) =& \frac{\hat{I}_{\mathrm{speak}n} N e^{j\theta_{\mathrm{is}n}}}{2T_0} \frac{e^{jn(\Phi+\pi)} - e^{jn\Phi}}{jnN\omega_0} \\ &+ \frac{\hat{I}_{\mathrm{speak}n}}{2T_0} \frac{e^{-j\theta_{\mathrm{is}n}} \left(e^{-j[nN+2M]\omega_0\left(\frac{\Phi}{2\pi}T_{\mathrm{s}}+\frac{1}{2}T_{\mathrm{s}}\right)} - e^{-j[nN+2M]\omega_0\left(\frac{\Phi}{2\pi}T_{\mathrm{s}}\right)}\right)}{-j\left[nN+2M\right]\omega_0} \\ &\times \sum_{l=0}^{N-1} e^{-j[nN+2M]2\pi\frac{l}{N}} \\ &- \frac{\hat{I}_{\mathrm{speak}n} N e^{j\theta_{\mathrm{is}n}}}{2T_0} \frac{e^{jn(\Phi+2\pi)} - e^{jn(\Phi+\pi)}}{jnN\omega_0} \\ &- \frac{\hat{I}_{\mathrm{speak}n}}{2T_0} \frac{e^{-j\theta_{\mathrm{is}n}} \left(e^{-j(nN+2M)\omega_0\left(\frac{\Phi}{2\pi}T_{\mathrm{s}}+T_{\mathrm{s}}\right)} - e^{-j(nN+2M)\omega_0\left(\frac{\Phi}{2\pi}T_{\mathrm{s}}+\frac{1}{2}T_{\mathrm{s}}\right)}\right)}{-j\left(nN+2M\right)\omega_0} \\ &\times \sum_{l=0}^{N-1} e^{-j(nN+2M)2\pi\frac{l}{N}}. \end{aligned} \tag{21}$$

Since the sigma terms in (21) are zero, it is further simplified to be

$$i_{\mathrm{r}}\left(j\omega_{\mathrm{p}}\right) = \frac{\hat{I}_{\mathrm{speak}n} N e^{j\theta_{\mathrm{is}n}}}{jnN2\pi} e^{jn\Phi}\left(e^{jn\pi} - 1\right). \tag{22}$$

It is found that the coefficient of the complex exponential Fourier series at ω_{p} is as follows:

$$i_{\mathrm{r}}\left(j\omega_{\mathrm{p}}\right) = -\frac{\hat{I}_{\mathrm{speak}n} e^{j\theta_{\mathrm{is}n}}}{jn\pi} e^{jn\Phi}. \tag{23}$$

According to (14), the complex Fourier coefficient of the $\omega_{\mathrm{p}}+n\omega_{\mathrm{s}}$ component in i_{s} is as follows:

$$i_{\mathrm{s}}[j(\omega_{\mathrm{p}}+n\omega_{\mathrm{s}})] = \frac{\hat{I}_{\mathrm{speak}n}}{2} e^{j\theta_{\mathrm{is}n}}. \tag{24}$$

Considering $n = \pm 1$, the transfer function from $i_{\mathrm{s}}[j(\omega_{\mathrm{p}}+\omega_{\mathrm{s}})]$ and $i_{\mathrm{s}}[j(\omega_{\mathrm{p}}-\omega_{\mathrm{s}})]$ to $i_{\mathrm{r}}(j\omega_{\mathrm{p}})$, denoted as $G_{\mathrm{ii\_-1}}$ and $G_{\mathrm{ii\_1}}$, respectively, are found to be

$$G_{\mathrm{ii\_1}} = \frac{i_{\mathrm{r}}(j\omega_{\mathrm{p}})}{i_{\mathrm{s}}[j(\omega_{\mathrm{p}}-\omega_{\mathrm{s}})]} = \frac{2}{j\pi} e^{-j\Phi} \tag{25}$$

$$G_{\mathrm{ii\_-1}} = \frac{i_{\mathrm{r}}(j\omega_{\mathrm{p}})}{i_{\mathrm{s}}[j(\omega_{\mathrm{p}}+\omega_{\mathrm{s}})]} = -\frac{2}{j\pi} e^{j\Phi}. \tag{26}$$

With (25) and (26), Fig. 7 gives the control diagram of the multifrequency model from i_{s} to i_{r}.

As for the output filter after rectification, the impedance of the C_{f}-R_{Ld} network is as follows:

$$Z_{\mathrm{RC}}(s) = \frac{R_{\mathrm{Ld}}}{1 + sR_{\mathrm{Ld}}C_{\mathrm{f}}}. \tag{27}$$

With (27), the output volage can be readily obtained as follows:

$$v_{\mathrm{o}}(j\omega_{\mathrm{p}}) = i_{\mathrm{r}}(j\omega_{\mathrm{p}}) Z_{\mathrm{RC}}(j\omega_{\mathrm{p}}) \tag{28}$$

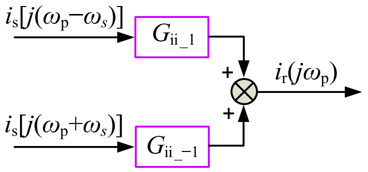

Fig. 7. Control diagram of the multifrequency model between i_{s} and i_{r} under primary-side regulation.

D. Small-Signal Expression of v_{CD}

Similarly, the expression of v_{CD} in a switching cycle is as follows:

$$v_{\mathrm{CD}}\left(t\right) = \begin{cases} -v_{\mathrm{o}} & \text{if } 0 \le t < \frac{\Phi}{2\pi}T_{\mathrm{s}} \\ v_o & \text{if } \frac{\Phi}{2\pi}T_{\mathrm{s}} \le t \le \frac{T_{\mathrm{s}}}{2} + \frac{\Phi}{2\pi}\ T_{\mathrm{s}} \\ -v_{\mathrm{o}} & \text{if } \frac{T_{\mathrm{s}}}{2} + \frac{\Phi}{2\pi}T_{\mathrm{s}} < t \le T_{\mathrm{s}}. \end{cases} \tag{29}$$

Performing Fourier transform on (29), the fundamental harmonic component of v_{CD} is expressed as follows:

$$v_{\mathrm{CD}}(t) = \frac{4}{\pi} v_{\mathrm{o}} \sin\left(\omega_{\mathrm{s}}t - \Phi\right). \tag{30}$$

Linearizing (30) around the equilibrium point leads to the small-signal component of v_{CD}, denoted as $\hat{v}_{\mathrm{CD}}(t)$, is as follows:

$$\hat{v}_{\mathrm{CD}}\left(t\right) \approx \frac{\partial v_{\mathrm{CD}}\left(t\right)}{\partial v_{\mathrm{o}}} \hat{v}_{\mathrm{o}} = \frac{4}{\pi} \hat{v}_{\mathrm{o}} \sin\left(\omega_{\mathrm{s}}t - \Phi\right). \tag{31}$$

With the perturbation of $\hat{\varphi}(t)$, the small-signal variable of the output voltage $\hat{v}_{\mathrm{o}}(t)$ contains the ω_{p} component, which can be expressed as follows:

$$\hat{v}_{\mathrm{o}}(t) = \hat{V}_{\mathrm{o}} \cos(\omega_{\mathrm{p}}t + \theta_{\mathrm{vo}}) = \frac{\hat{V}_{\mathrm{o}}}{2} e^{j\theta_{\mathrm{vo}}} e^{j\omega_{\mathrm{p}}t} + \frac{\hat{V}_{\mathrm{o}}}{2} e^{-j\theta_{\mathrm{vo}}} e^{-j\omega_{\mathrm{p}}t}. \tag{32}$$

Therefore, the small-signal expression of $\hat{v}_{\mathrm{CD}}(t)$ caused by $\hat{v}_{\mathrm{o}}(t)$ is as follows:

$$\begin{aligned} \hat{v}_{\mathrm{CD}}(t) &= \frac{4}{\pi} \hat{v}_{\mathrm{o}} \sin\left(\omega_{\mathrm{s}}t - \Phi\right) \\ &= -\frac{1}{j\pi} \hat{V}_{\mathrm{o}} e^{j(\theta_{\mathrm{vo}}+\Phi)} e^{j(\omega_{\mathrm{p}}-\omega_{\mathrm{s}})t} + \frac{1}{j\pi} \hat{V}_{\mathrm{o}} e^{-j(\theta_{\mathrm{vo}}+\Phi)} e^{j(\omega_{\mathrm{s}}-\omega_{\mathrm{p}})t} \\ &\quad + \frac{1}{j\pi} \hat{V}_{\mathrm{o}} e^{j(\theta_{\mathrm{vo}}-\Phi)} e^{j(\omega_{\mathrm{p}}+\omega_{\mathrm{s}})t} - \frac{1}{j\pi} \hat{V}_{\mathrm{o}} e^{-j(\theta_{\mathrm{vo}}-\Phi)} e^{-j(\omega_{\mathrm{s}}+\omega_{\mathrm{p}})t}. \end{aligned} \tag{33}$$

Hence, the Fourier coefficient of the $\omega_{\mathrm{p}} \pm \omega_{\mathrm{s}}$ component in $\hat{v}_{\mathrm{CD}}(t)$ is expressed as follows:

$$v_{\mathrm{CD}}[j(\omega_{\mathrm{p}} - \omega_{\mathrm{s}})] = -\frac{1}{j\pi} \hat{V}_{\mathrm{o}} e^{j(\theta_{\mathrm{vo}}+\Phi)} \tag{34}$$

$$v_{\mathrm{CD}}[j(\omega_{\mathrm{p}} + \omega_{\mathrm{s}})] = \frac{1}{j\pi} \hat{V}_{\mathrm{o}} e^{j(\theta_{\mathrm{vo}}-\Phi)}. \tag{35}$$

Considering the Fourier coefficient of the ω_{p} component in $\hat{v}_{\mathrm{o}}(t)$ below:

$$v_{\mathrm{o}}(j\omega_{\mathrm{p}}) = \frac{\hat{V}_{\mathrm{o}}}{2} e^{j\theta_{\mathrm{o}}} \tag{36}$$

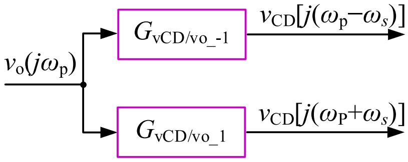

Fig. 8. Control block diagram of the multifrequency model from v_{o} to v_{CD} under primary-side regulation.

the transfer function from $v_{\mathrm{o}}(j\omega_{\mathrm{p}})$ to $v_{\mathrm{CD}}[j(\omega_{\mathrm{p}} \pm \omega_{\mathrm{s}})]$, defined as $G_{\mathrm{vCD/vo\_\pm 1}}$, is obtained as follows:

$$G_{\mathrm{vCD/vo\_-1}} = \frac{v_{\mathrm{CD}}[j(\omega_{\mathrm{p}} - \omega_{\mathrm{s}})]}{v_{\mathrm{o}}(j\omega_{\mathrm{p}})} = -\frac{2}{j\pi}e^{j\Phi}. \tag{37}$$

$$G_{\mathrm{vCD/vo\_1}} = \frac{v_{\mathrm{CD}}[j(\omega_{\mathrm{p}}+\omega_{\mathrm{s}})]}{v_{\mathrm{o}}(j\omega_{\mathrm{p}})} = \frac{2}{j\pi}e^{-j\Phi}. \tag{38}$$

The control block diagram of the multifrequency model from v_{in} to v_{AB} is depicted in Fig. 8.

E. Complete Multifrequency Model

Combining the control block diagrams in Figs. 4–8, the complete control block diagram from $\varphi(j\omega_p)$ to $v_o(j\omega_p)$ is finally obtained in Fig. 9.

On the basis of Fig. 9, the transfer function from $\varphi(j\omega_{\mathrm{p}})$ to $v_{\mathrm{o}}(j\omega_{\mathrm{p}})$, designated as $G_{\mathrm{v}\varphi}(j\omega_{\mathrm{p}})$ for primary-side regulation can be solved to be

$$\begin{aligned} G_{\mathrm{v}\varphi\_\mathrm{pri}}(j\omega_{\mathrm{p}}) &= \frac{v_{\mathrm{o}}(j\omega_{\mathrm{p}})}{\varphi(j\omega_{\mathrm{p}})} \\ &= \frac{4V_{\mathrm{in}}}{j\pi^2}\frac{Z_{\mathrm{RC}}(j\omega_{\mathrm{p}})\left(\frac{e^{-j\Phi}}{Z_{\mathrm{AB}}[j(\omega_{\mathrm{p}}-\omega_{\mathrm{s}})]} - \frac{e^{j\Phi}}{Z_{\mathrm{AB}}[j(\omega_{\mathrm{p}}+\omega_{\mathrm{s}})]}\right)}{1+\frac{4Z_{\mathrm{RC}}(j\omega_{\mathrm{p}})}{\pi^2}\left(\frac{1}{Z_{\mathrm{CD}}[j(\omega_{\mathrm{p}}-\omega_{\mathrm{s}})]}+\frac{1}{Z_{\mathrm{CD}}[j(\omega_{\mathrm{p}}+\omega_{\mathrm{s}})]}\right)}. \end{aligned} \tag{39}$$

Equation (39) is the analytic transfer function valid for all kinds of DAB resonant converters under primary-side regulation.

III. MODELING OF DAB RESONANT CONVERTER WITH SECONDARY SIDE REGULATION

When secondary-side regulation is employed, v_{AB} is fixed, whereas v_{CD} varies in accordance with the phase-shift angle φ. Consequently, the signal flow pattern alters, and the subsequent derivation is outlined below.

A. Small-Signal Expression of I_s

As observed in Fig. 2(b), the pathway from φ to v_{AB} is absent, having been supplanted by a new path from φ to v_{CD}. This implies that $v_{\mathrm{AB}}[j(\omega_{\mathrm{p}} \pm \omega_{\mathrm{s}})]$ equals zero. So, the model of the resonant tank is simplified to be

$$i_{\mathrm{s}}[j(\omega_{\mathrm{p}} - \omega_{\mathrm{s}})] = -\frac{v_{\mathrm{CD}}[j(\omega_{\mathrm{p}} - \omega_{\mathrm{s}})]}{Z_{\mathrm{CD}}[j(\omega_{\mathrm{p}} - \omega_{\mathrm{s}})]} \tag{40}$$

$$i_{\mathrm{s}}[j(\omega_{\mathrm{p}} + \omega_{\mathrm{s}})] = -\frac{v_{\mathrm{CD}}[j(\omega_{\mathrm{p}} + \omega_{\mathrm{s}})]}{Z_{\mathrm{CD}}[j(\omega_{\mathrm{p}} + \omega_{\mathrm{s}})]}. \tag{41}$$

The corresponding control block diagram of it is shown in Fig. 10.

B. Small-Signal Expression of I_r and V_o

Under secondary-side regulation, the relationship between i_{s} and i_{r} becomes

$$i_{\mathrm{r}}(t) = \begin{cases} i_{\mathrm{s}}(t) & \text{if } \frac{\varphi}{2\pi}T_{\mathrm{s}} \le t < \frac{\varphi}{2\pi}T_{\mathrm{s}} + \frac{1}{2}T_{\mathrm{s}} \\ -i_{\mathrm{s}}(t) & \text{if } \frac{\varphi}{2\pi}T_{\mathrm{s}} + \frac{1}{2}T_{\mathrm{s}} \le t < \frac{\varphi}{2\pi}T_{\mathrm{s}} + T_{\mathrm{s}} \end{cases}. \tag{42}$$

Unlike (17), changes in φ affect the zero-crossing instant of i_{r} directly, as illustrated in Fig. 11. This indicates that, besides being influenced by i_{s} [as shown in (25) and (26)], i_{r} also has a close relationship with φ, which will be derived below.

In Fig. 11, the steady-state value of i_{s} at T_φ is denoted as $I_{\mathrm{s}}(T_\varphi)$. At T_φ, i_{s} steps from $I_{\mathrm{s}}(T_\varphi)$ to $-I_{\mathrm{s}}(T_\varphi)$. Therefore, the small-signal component part of i_{r} caused by phase-shift angle change is approximated to be a pulse signal with the amplitude being $-2I_{\mathrm{s}}(T_\varphi)$ and the pulsewidth being be $\hat{\varphi}T_{\mathrm{s}}/2\pi$, which can be expressed as follows:

$$\hat{i}_{\mathrm{r}}(t) = \begin{cases} -2I_{\mathrm{s}}(T_\varphi) & \text{if } \frac{\Phi}{2\pi}T_{\mathrm{s}} \le t < \frac{\Phi}{2\pi}T_{\mathrm{s}}+\frac{\hat{\varphi}}{2\pi}T_{\mathrm{s}} \\ 0 & \text{if } \frac{\Phi}{2\pi}T_{\mathrm{s}}+\frac{\hat{\varphi}}{2\pi}T_{\mathrm{s}} \le t < \frac{\Phi}{2\pi}T_{\mathrm{s}} + \frac{T_{\mathrm{s}}}{2} \end{cases}. \tag{43}$$

Using the concept of periodic averaging, the quantitative relationship between $\hat{i}_{\mathrm{r}}$ and $\hat{\varphi}$ component is derived to be

$$\begin{aligned} \hat{i}_{\mathrm{r}}(t) &\approx \frac{2}{T_{\mathrm{s}}}\int_{\frac{\Phi}{2\pi}T_{\mathrm{s}}}^{\frac{\Phi}{2\pi}T_{\mathrm{s}}+\frac{T_{\mathrm{s}}}{2}} \hat{i}_{\mathrm{R}}(t)dt \\ &= \frac{2}{T_{\mathrm{s}}}\int_{\frac{\Phi}{2\pi}T_{\mathrm{s}}}^{\frac{\Phi}{2\pi}T_{\mathrm{s}}+\frac{\hat{\varphi}}{2\pi}T_{\mathrm{s}}} -2I_{\mathrm{s}}(T_\varphi)dt \\ &= -\frac{2I_{\mathrm{s}}(T_\varphi)}{\pi}\hat{\varphi}. \end{aligned} \tag{44}$$

So, the transfer function from $\hat{\varphi}$ to $\hat{i}_{\mathrm{r}}$ is as follows:

$$G_{\mathrm{ir}/\varphi} = \frac{i_{\mathrm{r}}(j\omega_{\mathrm{p}})}{\varphi(j\omega_{\mathrm{p}})} = -\frac{2I_{\mathrm{s}}(T_\varphi)}{\pi}. \tag{45}$$

Consequently, the actual $i_{\mathrm{r}}(j\omega_{\mathrm{p}})$ is the result of the superposition of (25), (26), and (45), as shown in Fig. 12.

C. Small-signal Expression of v_{CD}

As shown in Fig. 2(b), the expression of v_{CD} is as follows:

$$v_{\mathrm{CD}}(t) = \begin{cases} -v_o & \text{if } 0 \le t < \frac{\varphi}{2\pi}T_{\mathrm{s}} \\ v_o & \text{if } \frac{\varphi}{2\pi}T_{\mathrm{s}} \le t \le \frac{T_{\mathrm{s}}}{2} + \frac{\varphi}{2\pi}T_{\mathrm{s}} \\ -v_o & \text{if } \frac{T_{\mathrm{s}}}{2} + \frac{\varphi}{2\pi}T_{\mathrm{s}} < t \le T_{\mathrm{s}}. \end{cases} \tag{46}$$

Comparing to (29), it is apparent that apart from v_{o}, changes in φ also affect the v_{CD}. The relationship linking v_{o} and v_{CD} stays consistent with (37) and (38), while that between φ and v_{CD} is unique for secondary-side regulation. Further elaboration on this aspect will be provided subsequently.

The fundamental harmonic component of v_{CD} is as follows:

$$v_{\mathrm{CD}}(t) \approx \frac{4}{\pi}v_{\mathrm{o}}\sin(\omega_{\mathrm{s}}t - \varphi). \tag{47}$$

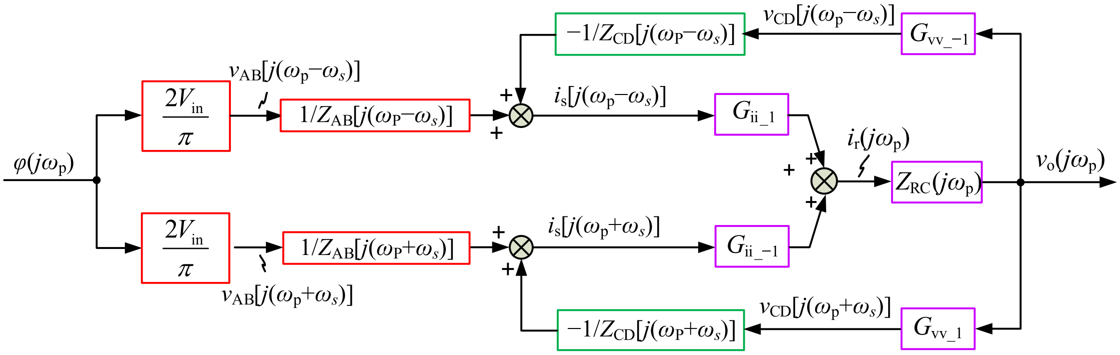

Fig. 9. Control block diagram of the general multifrequency small-signal model for resonant converter under primary side regulation.

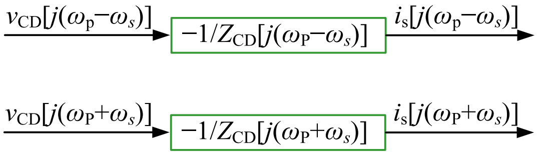

Fig. 10. General multifrequency small-signal model for resonant tank under secondary-side regulation.

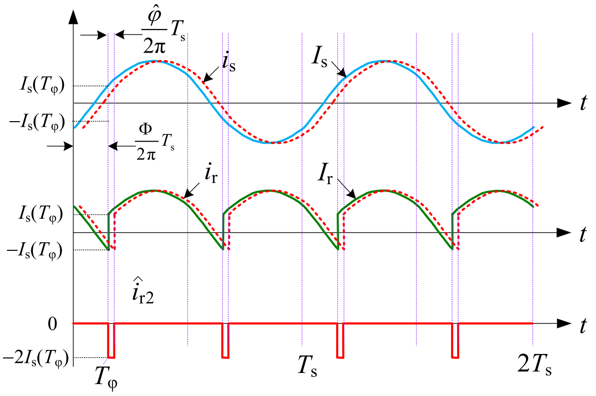

Fig. 11. Key waveforms of a DAB resonant converters under secondary side regulation.

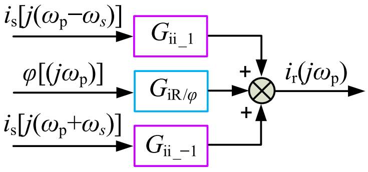

Fig. 12. Generation of small-signal component of i_r under secondary-side regulation.

Linearizing (47) leads to the following small-signal equation:

$$\hat{v}_{CD}(t) \approx \frac{\partial v_{CD}(t)}{\partial \varphi}\hat{\varphi} = -\frac{4}{\pi}V_o\hat{\varphi}\cos(\omega_s t - \Phi). \tag{48}$$

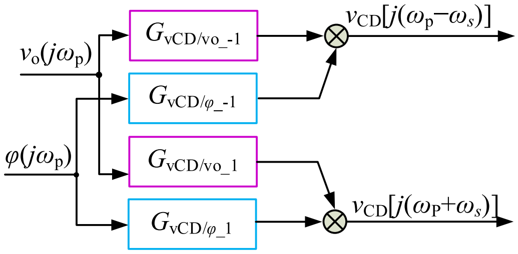

Fig. 13. Control block diagram of the multifrequency model from φ and v_o to v_{CD} under secondary-side regulation.

Considering the expression of $\hat{\varphi}(t)$ given in (4), $\hat{v}_{CD}(t)$ caused by $\hat{\varphi}(t)$ is as follows:

$$\begin{aligned}\hat{v}_{CD}(t) &= -\frac{4}{\pi}V_o\hat{\varphi}\cos(\omega_s t - \Phi)\\ &= -\frac{V_o}{\pi}\hat{\Phi}e^{j(\theta_\varphi+\Phi)}e^{j(\omega_p-\omega_s)t} - \frac{V_o}{\pi}\hat{\Phi}e^{-j(\theta_\varphi+\Phi)}e^{j(\omega_s-\omega_p)t}\\ &\quad - \frac{V_o}{\pi}\hat{\Phi}e^{j(\theta_\varphi-\Phi)}e^{j(\omega_p+\omega_s)t} - \frac{V_o}{\pi}\hat{\Phi}e^{-j(\theta_\varphi-\Phi)}e^{-j(\omega_s+\omega_p)t}.\end{aligned} \tag{49}$$

The Fourier coefficients of the $\omega_p \pm \omega_s$ component in $\hat{v}_{CD}(t)$ are expressed as follows:

$$v_{CD}[j(\omega_p-\omega_s)] = -\frac{V_o}{\pi}\hat{\Phi}e^{j(\theta_\varphi+\Phi)} \tag{50}$$

$$v_{CD}[j(\omega_p+\omega_s)] = -\frac{V_o}{\pi}\hat{\Phi}e^{j(\theta_\varphi-\Phi)}. \tag{51}$$

Considering the Fourier coefficient of the ω_p component in $\hat{\varphi}(t)$ is $\varphi(j\omega_p) = \frac{\hat{\Phi}}{2}e^{j\theta_\varphi}$. Therefore, the transfer function from $\varphi(j\omega_p)$ to $v_{CD}[j(\omega_p \pm \omega_s)]$, defined as $G_{vCD/\varphi\_\pm1}$, is obtained as follows:

$$G_{vCD/\varphi\_-1} = \frac{v_{CD}[j(\omega_p-\omega_s)]}{\varphi(j\omega_p)} = -\frac{2V_o}{\pi}e^{j\Phi} \tag{52}$$

$$G_{vCD/\varphi\_1} = \frac{v_{CD}[j(\omega_p+\omega_s)]}{\varphi(j\omega_p)} = -\frac{2V_o}{\pi}e^{-j\Phi}. \tag{53}$$

Equations (52) and (53), along with (37) and (38), collectively form the final control block diagram, which is depicted in Fig. 13.

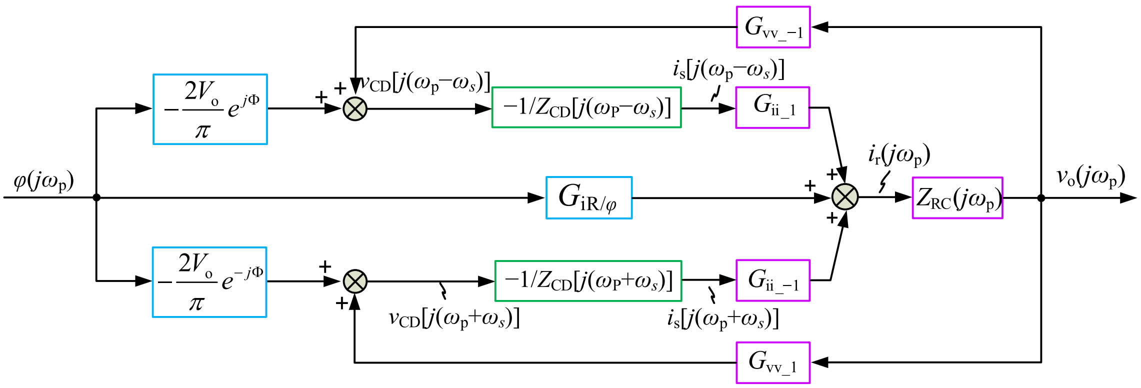

Fig. 14. Control block diagram of the general multifrequency small-signal model for resonant converter under secondary-side regulation.

D. Complete Multifrequency Model

Combining the submodules' models, the complete control block diagram of DAB resonant converter under secondary-side regulation is finally obtained as Fig. 14. Equation (54) is the expected analytic transfer function valid for DAB resonant converters with various resonant tanks.

$$G_{\mathrm{v}\varphi\_\mathrm{sec}}(s) = \frac{v_{\mathrm{o}}(j\omega_{\mathrm{p}})}{\varphi(j\omega_{\mathrm{p}})}$$
$$= Z_{\mathrm{RC}}(j\omega_{\mathrm{p}})\frac{\frac{-2I_{\mathrm{s}}(T_\varphi)}{\pi}+\frac{4V_{\mathrm{o}}}{j\pi^2}\left(\frac{1}{Z_{\mathrm{CD}}[j(\omega_{\mathrm{p}}-\omega_{\mathrm{s}})]}-\frac{1}{Z_{\mathrm{CD}}[j(\omega_{\mathrm{p}}+\omega_{\mathrm{s}})]}\right)}{1+\frac{4}{\pi^2}Z_{\mathrm{RC}}(j\omega_{\mathrm{p}})\left(\frac{1}{Z_{\mathrm{CD}}[j(\omega_{\mathrm{p}}+\omega_{\mathrm{s}})]}+\frac{1}{Z_{\mathrm{CD}}[j(\omega_{\mathrm{p}}-\omega_{\mathrm{s}})]}\right)} \tag{54}$$

where

$$I_{\mathrm{s}}(T_\varphi)$$
$$= \frac{4V_{\mathrm{in}}}{\pi\left|Z_{\mathrm{AB}}(j\omega_{\mathrm{s}})\right|}\left[\sin\left(\Phi-\Theta_{\mathrm{AB}}\right)+\frac{\cos\left(\Phi-\Theta_{\mathrm{AB}}\right)\sin\Theta_{\mathrm{CD}}}{\frac{\left|Z_{\mathrm{CD}}(j\omega_{\mathrm{s}})\right|}{R_{\mathrm{eq}}}+\cos\Theta_{\mathrm{CD}}}\right] \tag{55a}$$

$$V_{\mathrm{o}} = V_{\mathrm{in}}\frac{\frac{R_{\mathrm{eq}}}{\left|Z_{\mathrm{AB}}(j\omega_{\mathrm{s}})\right|}\cos\left(\Phi-\Theta_{\mathrm{AB}}\right)}{1+\frac{R_{\mathrm{eq}}}{\left|Z_{\mathrm{CD}}(j\omega_{\mathrm{s}})\right|}\cos\left(\Theta_{\mathrm{CD}}\right)}. \tag{55b}$$

IV. EXAMPLE AND DISCUSSION

A. Model Applicability to Different Resonant Tanks

Among the numerous DAB resonant converters, the DABSRC and the DAB *CLLC* converter are the most prevalent. Here, we will take these two converters as examples to showcase the effectiveness of the proposed model for DAB converters with various resonant tanks.

The corresponding resonant tank of DABSRC is shown in Fig. 15(a), from which, the expressions of $Z_{\mathrm{AB}}(s)$ and $Z_{\mathrm{CD}}(s)$ are readily solved to be

$$Z_{\mathrm{AB}}(s) = Z_{\mathrm{CD}}(s) = \mathrm{s}L_{\mathrm{r}}+\frac{1}{sC_{\mathrm{r}}}+R_{\mathrm{r}}. \tag{56}$$

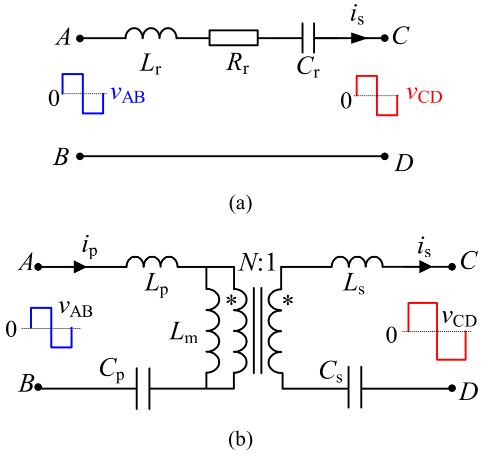

(a)

(b)

Fig. 15. Two-port network representation of different resonant tanks. (a) DABSRC. (b) DAB *CLLC* converter.

As for the *CLLC* resonant tank in Fig. 15(b), this derivation process is relatively complex. Converting the secondary side impedance of the resonant tank to the primary side, and then employing the superposition theorem, we can finally obtain the expressions for $Z_{\mathrm{AB}}(s)$ and $Z_{\mathrm{CD}}(s)$ as follows:

$$Z_{\mathrm{AB}}(s) = N\frac{\left(sL_{\mathrm{s}}+\frac{1}{sC_{\mathrm{s}}}+\frac{sL_{\mathrm{m}}}{N^2}\right)\left(sL_{\mathrm{p}}+\frac{1}{sC_{\mathrm{p}}}\right)}{sL_{\mathrm{m}}}$$
$$+N\left(sL_{\mathrm{s}}+\frac{1}{sC_{\mathrm{s}}}\right) \tag{57a}$$

$$Z_{\mathrm{CD}}(s) = sL_{\mathrm{s}}+\frac{1}{sC_{\mathrm{s}}}-\frac{1}{N^2}\left(\frac{s^2{L_{\mathrm{m}}}^2}{s\left(L_{\mathrm{m}}+L_{\mathrm{p}}\right)+\frac{1}{sC_{\mathrm{s}}}}-sL_{\mathrm{m}}\right). \tag{57b}$$

A set of circuit parameters for DABSRC converter and DAB *CLLC* converter are designed, as tabulated in Tables I and II, respectively. Incorporating these values into the model, the transfer functions from the phase-shift angle to the output voltage can be obtained. These results are depicted in Figs. 16 and 17, accompanied by corresponding Simplis simulation results.

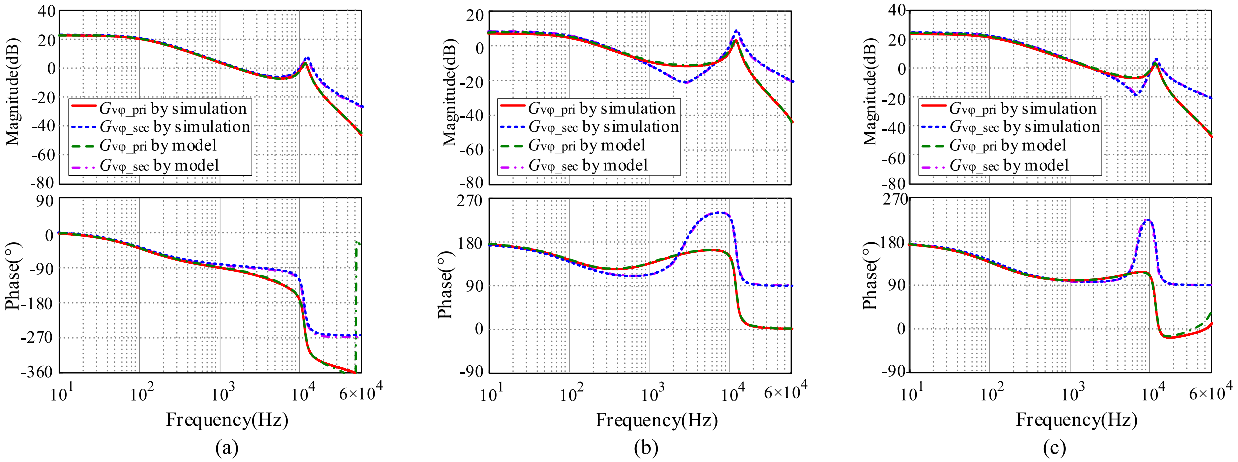

Fig. 16. Bode diagrams of $G_{\mathrm{v}\varphi}$ of the DABSRC by the proposed model and by simulation when (a) $\Phi = 0.3\pi$, (b) $\Phi = 0.5\pi$, and (c) $\Phi = 0.7\pi$.

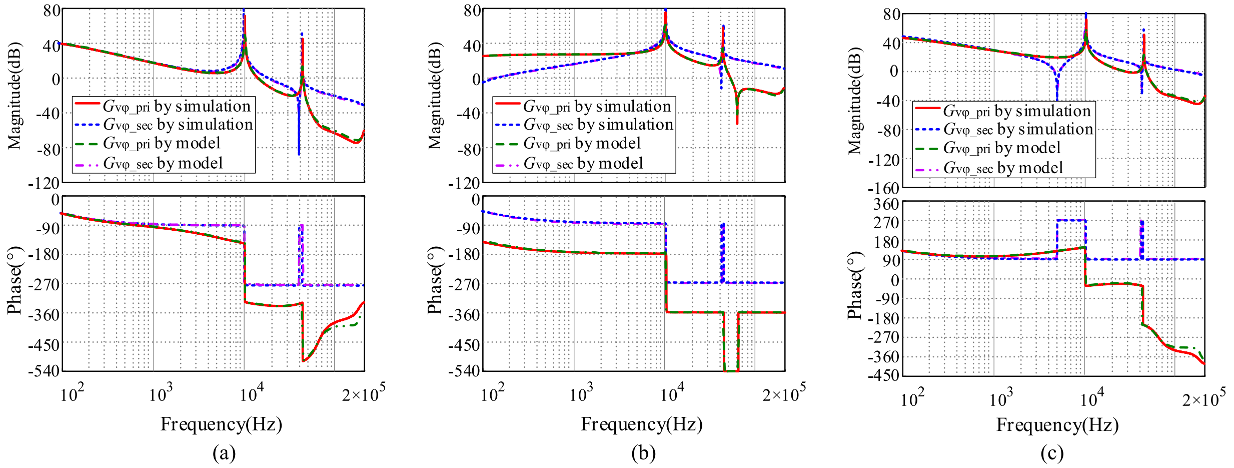

Fig. 17. Bode diagrams of $G_{\mathrm{v}\varphi}$ of the DAB *CLLC* converter by the proposed model and by simulation when (a) $\Phi = 0.3\pi$, (b) $\Phi = 0.5\pi$, and (c) $\Phi = 0.7\pi$.

TABLE I
Parameters of the DABSRC

Parameters	Values	Parameters	Values
V_{in}	15 V	C_{f}	22 μF
f_{s}	57 kHz	R_{Ld}	3 Ω
L_{r}	211 μH	Φ	0.39π
C_{r}	51 nF	V_{m}	5 V
R_{r}	2.53 Ω	H_{v}	0.601

TABLE II
Parameters of the DAB *CLLC* Converter

Parameters	Values	Parameters	Values
V_{in}	400V	L_{s}	128.5 μH
L_{p}	185 μH	C_{s}	13.68 nF
f_{s}	125 kHz	N	1.2
C_{p}	50 nF	C_{o}	22 μF
L_{m}	83.2 μH	R_{Ld}	90 Ω

Notably, within the range of the switching frequency, the theoretical results, both $G_{\mathrm{v}\varphi\_\mathrm{pri}}$ and $G_{\mathrm{v}\varphi\_\mathrm{sec}}$, matched closely with that by simulation results. This underscores the universal applicability of the proposed model to different DAB resonant converters.

B. Difference Between Primary and Secondary-Side Regulation

It is evidently found from the previous text that primary-side and secondary-side regulation exhibit significant differences. Based on the derivations, Fig. 18 summarizes the signal flow graphs for both regulations, revealing the differences in the relationships between the phase-shift angle and v_{AB}, v_{CD}, i_{s}, and i_{r}. Ultimately, this results in different transfer functions from the phase-shift angle to the output voltage for primary-side and secondary-side regulation. To further distinguish the differences, the DABSRC is taken as an example here.

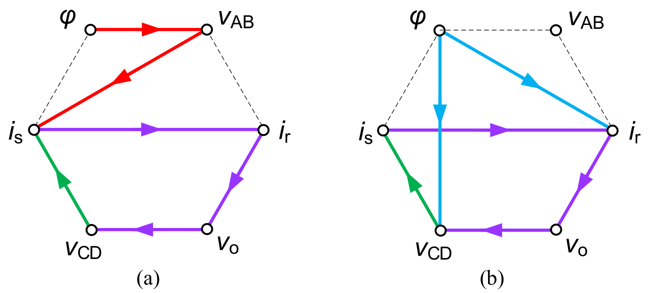

(a) (b)

Fig. 18. Small-signal-flow graphs for primary side regulation and secondary side regulation of a DAB resonant converter. (a) Primary-side regulation. (b) Secondary-side regulation.

For the purpose of facilitating analysis, the model is simplified, with the simplification process detailed in Appendix Section. The final approximated expressions of $G_{\mathrm{v}\varphi\_\mathrm{pri}}(s)$ and $G_{\mathrm{v}\varphi\_\mathrm{sec}}(s)$ are as follows:

$$G_{\mathrm{v}\varphi\_\mathrm{pri}}(s) = \frac{V_{\mathrm{in}} R_{\mathrm{eq}}\left[-sL_{\mathrm{r}}K_{\mathrm{eq}}\sin(\Phi) + X_{\mathrm{eq}}\cos(\Phi) - R_{\mathrm{r}}\sin(\Phi)\right]}{\left(Z_{\mathrm{eq}}^2 + 2s^2L_{\mathrm{r}}^2K_{\mathrm{eq}} + 2sR_{\mathrm{r}}L_{\mathrm{r}} + \frac{2sR_{\mathrm{r}}}{\omega_{\mathrm{s}}^2C_{\mathrm{r}}}\right) \times (1 + sC_{\mathrm{o}}R_{\mathrm{Ld}}) + (sL_{\mathrm{r}}K_{\mathrm{eq}} + R_{\mathrm{r}})R_{\mathrm{eq}}} \tag{58}$$

$$G_{\mathrm{v}\varphi\_\mathrm{sec}}(s) = \frac{R_{\mathrm{eq}}}{Z_{\mathrm{eq}}} \cdot \frac{-\left[V_{\mathrm{in}}\sin(\Phi - \Theta_{\mathrm{Zr}}) + V_{\mathrm{o}}\sin\Theta_{\mathrm{Zr}}\right]\left(Z_{\mathrm{eq}}^2 + 2s^2L_{\mathrm{r}}^2K_{\mathrm{eq}} + 2sR_{\mathrm{r}}L_{\mathrm{r}} + \frac{2sR_{\mathrm{r}}}{\omega_{\mathrm{s}}^2C_{\mathrm{r}}}\right) + Z_{\mathrm{eq}}V_{\mathrm{o}}X_{\mathrm{eq}}}{\left(Z_{\mathrm{eq}}^2 + 2s^2L_{\mathrm{r}}^2K_{\mathrm{eq}} + 2sR_{\mathrm{r}}L_{\mathrm{r}} + \frac{2sR_{\mathrm{r}}}{\omega_{\mathrm{s}}^2C_{\mathrm{r}}}\right) \times (1 + sC_{\mathrm{o}}R_{\mathrm{Ld}}) + (sL_{\mathrm{r}}K_{\mathrm{eq}} + R_{\mathrm{r}})R_{\mathrm{eq}}} \tag{59}$$

where $s = j\omega_{\mathrm{p}}, X_{\mathrm{eq}} = \omega_{\mathrm{s}}L_{\mathrm{r}} - \frac{1}{\omega_{\mathrm{s}}C_{\mathrm{r}}}$, $Z_{\mathrm{eq}} = \sqrt{X_{\mathrm{eq}}^2 + R_{\mathrm{r}}^2}$, $R_{\mathrm{eq}} = \frac{8}{\pi^2}R_{\mathrm{Ld}}$, $K_{\mathrm{eq}} = (1 + \frac{1}{\omega_{\mathrm{s}}^2L_{\mathrm{r}}C_{\mathrm{r}}})$, $V_{\mathrm{o}} = V_{\mathrm{in}}\frac{R_{\mathrm{eq}}\cos(\Theta_{Zr} - \Phi)}{|Z_{\mathrm{r}}(j\omega_{\mathrm{s}})| + R_{\mathrm{eq}}\cos(\Theta_{Zr})}$, and $\Theta_{\mathrm{Zr}} = \arctan X_{\mathrm{eq}}/R_{\mathrm{r}}$.

From (58) and (59), it can be seen that $G_{\mathrm{v}\varphi\_\mathrm{pri}}(s)$ and $G_{\mathrm{v}\varphi\_\mathrm{sec}}(s)$ share the same poles, but the zeros are different, which will result in significant differences in the dynamic performance. The zeros will be solved here for comparison. To ensure the generality, the normalization of the zeros is performed. For $G_{\mathrm{v}\varphi\_\mathrm{pri}}(s)$, the zero is found to be

$$z_{\mathrm{pri}} = \frac{(f_{\mathrm{n}}^2 - 1)f_{\mathrm{n}}\omega_{\mathrm{r}}}{(f_{\mathrm{n}}^2 + 1)\tan\Phi} \tag{60}$$

while $G_{\mathrm{v}\varphi\_\mathrm{sec}}(s)$ has a pair of conjugate zeros as follows:

$$z_{\mathrm{sec}1,2} = \frac{(f_{\mathrm{n}}^2 - 1)}{(f_{\mathrm{n}}^2 + 1)} \frac{\pm\omega_{\mathrm{r}}\sqrt{\frac{(f_{\mathrm{n}}^2+1)Q}{(f_{\mathrm{n}}^2-1)f_{\mathrm{n}}}\left[\sin(2\Phi) - 2Q\cos^2(\Phi)\left(f_{\mathrm{n}} - \frac{1}{f_{\mathrm{n}}}\right)\right]}}{2\left[\sin(\Phi) - Q\cos(\Phi)\left(f_{\mathrm{n}} - \frac{1}{f_{\mathrm{n}}}\right)\right]} \tag{61}$$

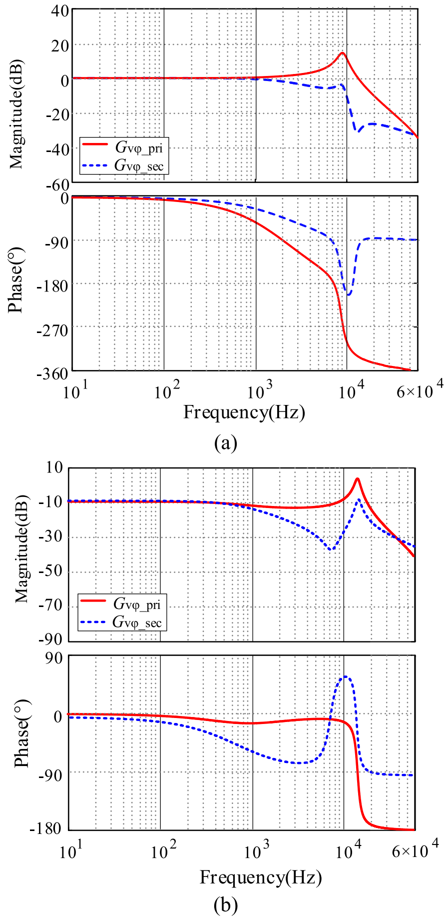

(a)

(b)

Fig. 19. Two possible relationships between $G_{\mathrm{v}\varphi\_\mathrm{pri}}$ and $G_{\mathrm{v}\varphi\_\mathrm{sec}}$ of the DABSRC. (a) $G_{\mathrm{v}\varphi\_\mathrm{sec}}$ is ahead of $G_{\mathrm{v}\varphi\_\mathrm{pri}}$ in phase at low frequencies @ $\Phi = 0.5\pi, f_{\mathrm{s}} = 63.5$ kHz, $R_{\mathrm{Ld}} = 10\Omega$. (b) $G_{\mathrm{v}\varphi\_\mathrm{pri}}$ is ahead of $G_{\mathrm{v}\varphi\_\mathrm{sec}}$ in phase at low frequencies @ $\Phi = 0.39\pi, f_{\mathrm{s}} = 57$ kHz, $R_{\mathrm{Ld}} = 3\Omega$.

where

$$f_{\mathrm{n}} = \frac{f_{\mathrm{s}}}{f_{\mathrm{r}}} = \frac{\omega_{\mathrm{s}}}{\omega_{\mathrm{r}}}, Q = \frac{1}{R_{\mathrm{eq}}}\sqrt{\frac{L_{\mathrm{r}}}{C_{\mathrm{r}}}}. \tag{62}$$

It can be observed that the zeros are closely correlated with f_{n}, Φ, and Q. For primary-side regulation, z_{pri} is a real root. Considering that the switching frequency is usually greater than the resonant frequency for DABSRC, i.e., $f_{\mathrm{n}} > 1$, the size and sign of z_{pri} is determined by Φ. When Φ approaches 0.5π from 0, z_{pri} is located in the right half plane and gradually approaches the origin; when Φ approaches π from 0.5 π, z_{pri} is located in the left half plane and away from the origin. However, the intricate relationships between $z_{\mathrm{sec}1,2}$ and f_{n}, Φ, Q inherently produce transcendental equations during solving, which precludes precise quantitative analysis. Therefore, it is exceedingly challenging to quantitatively discern the superiority between $G_{\mathrm{v}\varphi\_\mathrm{pri}}(s)$ and $G_{\mathrm{v}\varphi\_\mathrm{sec}}(s)$. But after extensive numerical analysis and simulation, it is found that $G_{\mathrm{v}\varphi\_\mathrm{pri}}(s)$ and $G_{\mathrm{v}\varphi\_\mathrm{sec}}(s)$ have two possible relationships from the curves, as illustrated in Fig. 19(a) and (b), with the majority corresponding to Fig. 19(a) and rare instances resembling Fig. 19(b). Obviously, the scenario in Fig. 19(a) shows $G_{\mathrm{v}\varphi\_\mathrm{sec}}(s)$ has better phase characteristics

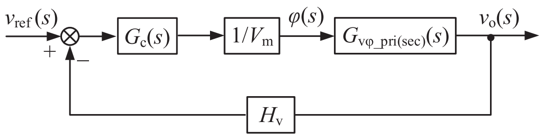

Fig. 20. Closed-loop control block diagram of the DABSRC system.

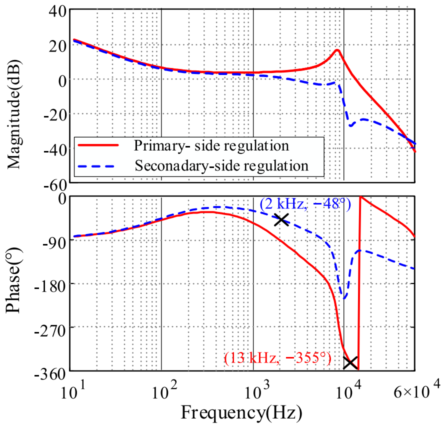

Fig. 21. Loop gain curve of the DABSRC using controller in (64) according to the proposed model.

than $G_{\mathrm{v}\varphi\_\mathrm{pri}}(s)$, indicating that secondary-side regulation is easier to achieve good stability and dynamic performance. The scenario in Fig. 19(b) shows that $G_{\mathrm{v}\varphi\_\mathrm{pri}}(s)$ exhibits superior phase characteristics compared to $G_{\mathrm{v}\varphi\_\mathrm{sec}}(s)$ at low frequencies, but has a more pronounced resonant peak in the mid-frequency range [16 kHz in Fig. 19(b)]. This heightened resonance peak of $G_{\mathrm{v}\varphi\_\mathrm{pri}}(s)$ may potentially induce multiple crossing in the loop gain after compensation, risking the stability of the system. As a result, secondary-side regulation is still better than primary-side regulation, unless the latter uses other control methods to dampen its resonance peak.

In conclusion, secondary-side regulation generally surpasses primary-side regulation for DABSRC. However, in practical design, it is advisable to draw both transfer functions according to the specific circuit parameters first, and then select the optimal regulation method.

On the basis of the open loop transfer function in Fig. 19(a), a closed loop system in the form of Fig. 20 is designed, where $1/\mathrm{V}_{\mathrm{m}}$ is the gain of the phase-shift modulator, H_{v} is the voltage sensor, and $G_{\mathrm{c}}(\mathrm{s})$ is the compensator parameter.

The loop-gain expressions for both primary-side and secondary-side regulations are as follows:

$$T_{\mathrm{pri(sec)}}(s) = \frac{1}{V_{\mathrm{m}}} H_{\mathrm{v}} G_{\mathrm{c}}(s) G_{\mathrm{v}\varphi\_\mathrm{pr(sec)}}(s). \tag{63}$$

For the main circuit parameters in Table I, set the expected output voltage to 1.65 V, the compensator parameter $G_{\mathrm{c}}(s)$ to

$$G_{\mathrm{c}}(s) = 1243 \frac{\left(1+\frac{s}{200\pi}\right)}{s\left(1+\frac{s}{60000\pi}\right)}. \tag{64}$$

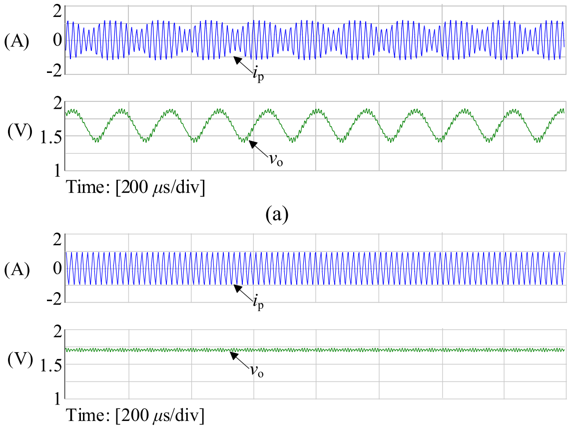

(a)

(b)

Fig. 22. Simulation waveforms of the closed-loop DABSRC with different phase-shift schemes. (a) Primary-side regulation, unstable. (b) Secondary-side regulation, stable.

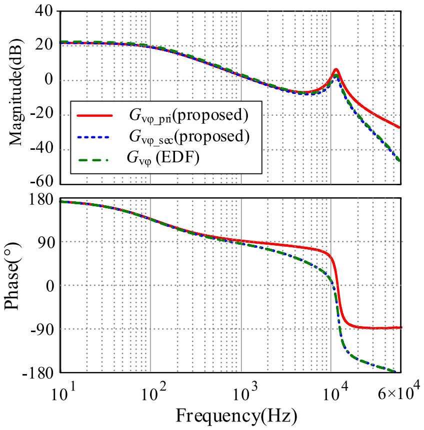

Fig. 23. Comparison of the transfer functions of $G_{\mathrm{v}\varphi}$ by EDF method and the multifrequency method when $\Phi = 0.3\pi$.

Fig. 21 displays the Bode plots of the corresponding loop gains. It can be observed that the cut-off frequency and phase margin for primary-side regulation are 13 kHz and −175°. There exists a negative crossover at approximately 6 kHz. As for secondary-side regulation, they are 2 kHz and 132°, and there is no crossover. This indicates that the system should be unstable in the former case but stable in the latter according to Nyquist criterion. The time-domain simulation waveforms presented in Fig. 22 aligns perfectly with the prediction by proposed model, thereby validating the difference between primary-side regulation and secondary-side regulation in control loop design and stability assessment.

C. Comparison With Other Modeling Methods

Other popular modeling methods available for DAB resonant converters include the GSSA, EDF, and LPT methods, whose core idea is to find a set of slow variables with dc operating points to depict the pure ac variables in the resonant tank. These

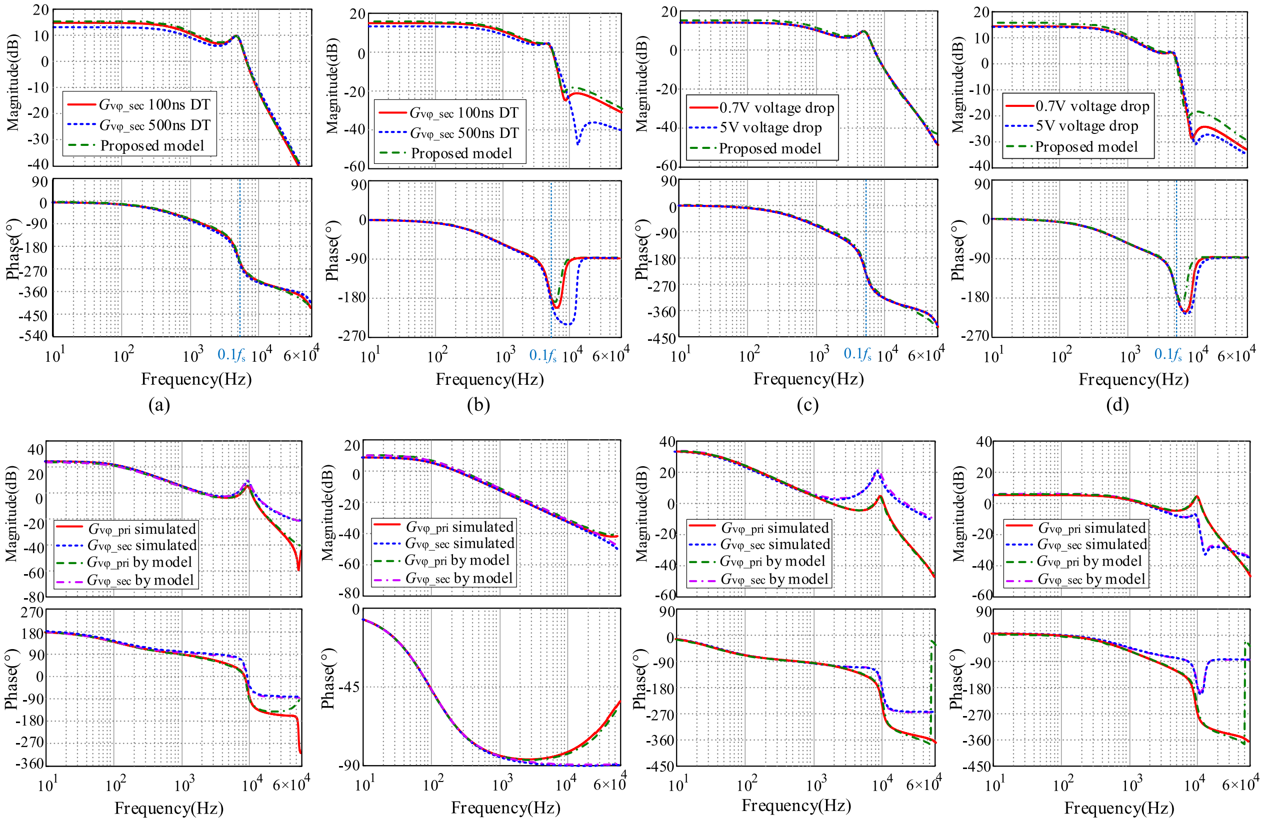

(a) (b) (c) (d)

(e) (f) (g) (h)

Fig. 24. Illustration of the proposed model's accuracy considering different circuit parameters. (a) and (b) Results when the dead time is 100 ns and 500 ns, respectively, @ $\Phi = 0.2\pi, f_{\rm n} = 1.1$. (c) and (d) Results when the forward voltage drop of diode is 0.7 V and 5 V, respectively, @ $\Phi = 0.2\pi, f_{\rm n} = 1.1$. (e) and (f) are the results when $f_{\rm n} = 0.8, 3$, respectively, @$\Phi = 0.3\pi$, $R_{\rm Ld} = 10\Omega$. (g) and (h) Results when the Q value is 0.1 and 10, respectively @ $\Phi = 0.2\pi, f_{\rm n} = 1.1$.

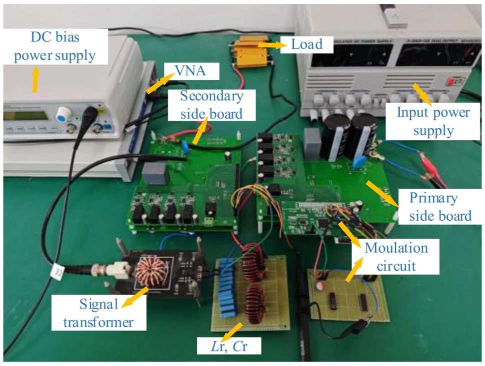

Fig. 25. Test platform for transfer function measurement.

methods are essentially equivalent. Here, a comparison with the EDF method is made.

When using EDF method, a nonlinear state-space representation of the converter is built first. Then, all the state variables in the resonant tank are decomposed into sine term and cosine term as follows:

$$x_i(t) = x_{is}(t)\sin(\omega_{\rm s} t) + x_{ic}(t)\cos(\omega_{\rm s} t), i = 1, 2, \ldots n \tag{65}$$

where $x_{is}(t)$ and $x_{ic}(t)$ are dc values in steady state, but vary slowly around the dc values when perturbed. By substituting (65) into the nonlinear state-space representation and subsequently applying harmonic balance combined with local linearization techniques, we can obtain the following linearized small-signal (66), (67), with $x_{is}(t)$ and $x_{ic}(t)$ and the output capacitor voltage $v_{\rm Cf}$ being the new state variables.

$$\frac{d}{dt}\begin{bmatrix}\hat{\mathbf{x}}_{\rm s}\\ \hat{\mathbf{x}}_{\rm c}\\ \hat{v}_{\rm Cf}\end{bmatrix} = \mathbf{A}_{\rm ss}\begin{bmatrix}\hat{\mathbf{x}}_{\rm s}\\ \hat{\mathbf{x}}_{\rm c}\\ \hat{v}_{\rm Cf}\end{bmatrix} + \mathbf{B}_{\rm ss}\hat{\varphi} \tag{66}$$

$$\hat{v}_{\rm o} = \mathbf{C}_{\rm ss}\begin{bmatrix}\hat{\mathbf{x}}_{\rm s}\\ \hat{\mathbf{x}}_{\rm c}\\ \hat{v}_{\rm Cf}\end{bmatrix} \tag{67}$$

where $\mathbf{A_{ss}}$, $\mathbf{B_{ss}}$, and $\mathbf{C_{ss}}$ are the coefficient matrices of the equations.

Finally, the transfer function $G_{{\rm v}\varphi}(j\omega_{\rm p})$ are obtained via Laplace Transform as follows:

$$G_{{\rm v}\varphi}(j\omega_p) = \mathbf{C}_{\rm ss}(s\mathbf{I} - \mathbf{A}_{\rm ss})^{-1}\mathbf{B}_{\rm ss}. \tag{68}$$

In light of the fact that existing literature, such as [9] and [10], predominantly addresses small-signal modeling of DABSRC, this work adopts DABSRC as the representative case study for subsequent comparison. For DABSRC, the new state variables are

$$\begin{bmatrix}\hat{\mathbf{x}}_{\rm s} & \hat{\mathbf{x}}_{\rm c} & \hat{v}_{\rm Cf}\end{bmatrix} = \begin{bmatrix}\hat{i}_{\rm Lrs} & \hat{v}_{\rm Crs} & \hat{i}_{\rm Lrc} & \hat{v}_{\rm Crs} & \hat{v}_{\rm Cf}\end{bmatrix}. \tag{69}$$

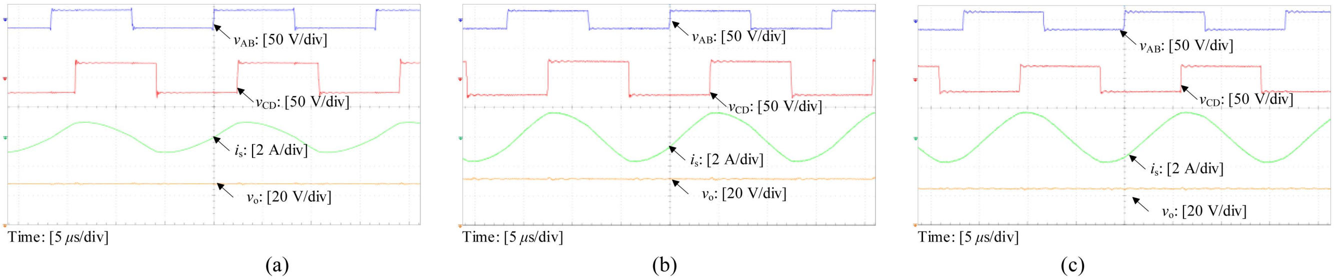

Fig. 26. Steady-state time-domain experimental waveforms of the DABSRC. (a) $\Phi = 0.3\pi$, (b) $\Phi = 0.5\pi$, (c) $\Phi = 0.7\pi$, respectively.

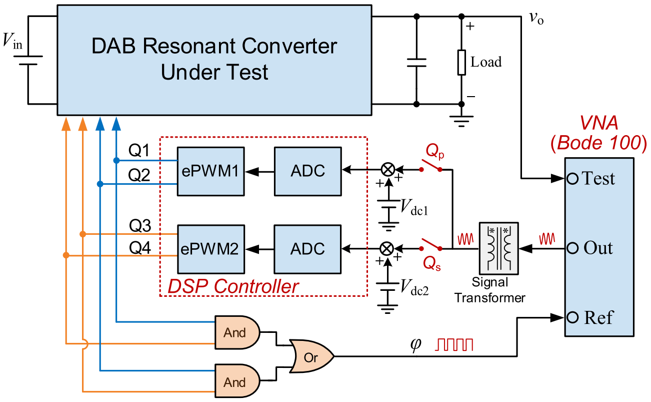

Fig. 27. Schematic diagram of the measurement of $G_{v\varphi}(s)$.

The coefficients matrices have been derived to be

$$\mathbf{A}_{ss} = \begin{bmatrix} \frac{-R_r}{L_r} & \omega_s & \frac{-1}{L_r} & 0 & -\frac{4}{\pi L_r}\cos(\Phi) \\ \frac{1}{C_r} & 0 & 0 & \omega_s & 0 \\ -\omega_s & \frac{-R_r}{L_r} & 0 & \frac{-1}{L_r} & \frac{4}{\pi L_r}\sin(\Phi) \\ 0 & \frac{1}{C_r} & -\omega_s & 0 & 0 \\ \frac{2}{\pi C_f}\cos\Phi & -\frac{2}{\pi C_f}\sin\Phi & 0 & 0 & -\frac{1}{C_f R_{Ld}} \end{bmatrix} \tag{70}$$

$$\mathbf{B}_{ss} = \begin{bmatrix} \frac{4}{\pi L_r} V_o \sin(\Phi) \\ 0 \\ \frac{4}{\pi L_r} V_o \cos(\Phi) \\ 0 \\ -\frac{2}{\pi C_f}\left[I_{Lrs}\sin(\Phi) + I_{Lrc}\cos(\Phi)\right] \end{bmatrix} \tag{71}$$

$$\mathbf{C}_{ss} = \begin{bmatrix} 0 & 0 & 0 & 0 & 1 \end{bmatrix} \tag{72}$$

where I_{Lrs}, I_{Lrc}, V_{Crs}, V_{Crc}, and V_o are the corresponding steady-state values of the new state variables.

By substituting (70)–(72) into (66) and (67), the EDF-based transfer functions of the DABSRC can be obtained and illustrated in Fig. 21 for comparative analysis against the proposed model. It reveals that the EDF model coincides with the secondary-side regulation, but it loses the result of primary-side regulation. This discrepancy arises from an inherent limitation in conventional phase-shift control modeling approaches—specifically, the prevalent assumption that adopts v_{AB} as the fixed reference frame, where v_{AB} remains stationary while v_{CD} varies with perturbation. Consequently, the intricate coupling relationship between v_{AB} and phase-shift angle perturbation is overlooked, inadvertently discarding a valid dynamic model that could otherwise account for primary-side regulation.

In addition, the implementation of EDF method involves decomposing each state variable into sine term and cosine term when modeling the resonant tank. This decomposition necessitates the individual derivation of state equations for each newly created variable, leading to a significant proliferation of equations. Specifically, for an Nth-order resonant converter incorporating output filtering capacitors, the total number of state equations escalates to $2N+1$. This becomes prohibitively complex when applied to high-order resonant topologies, severely limiting its practical applicability. The decomposition of resonant variables one by one also makes it difficult to intuitively reflect the overall dynamic characteristics inside the resonant tank, masking the subtle inherent relationships between resonant elements, and posing obstacles to the simplification of the model. In contrast, the methodology proposed herein depicts the model of resonant tank using just two impedance parameters Z_{AB} and Z_{CD}, which can be easily obtained for various high-order resonant converters, based on which, a unified transfer function for various DAB resonant converters with different resonant tanks is derived. Therefore, this modeling method greatly simplifies the modeling process and is very friendly to high-order resonant converters. Also, as it treats the entire resonant network as a whole, the inherent coupling between resonant elements is well preserved.

D. *Effect of the Parameters on the Accuracy of the Model*

This section will study the impact of circuit parameters as well as some overlooked parameters on model accuracy. The parameters are basically consistent with Table I, while the differences have been marked in the title of Fig. 24.

1) Effect of the Dead Time: The dead time (DT) is ignored while modeling. Fig. 24(a) and (b) have a comparison of the proposed model with the simulation results at different dead times. It shows that the dead time has little effect on $G_{v\varphi\_pri}(s)$ up to the switching frequency. In contrast, $G_{v\varphi\_sec}(s)$ coincides well with the model below 1/10 of the switching frequency, but at higher frequency range, it has some error. The main reason is that the dead time changes the turn-ON instant of the

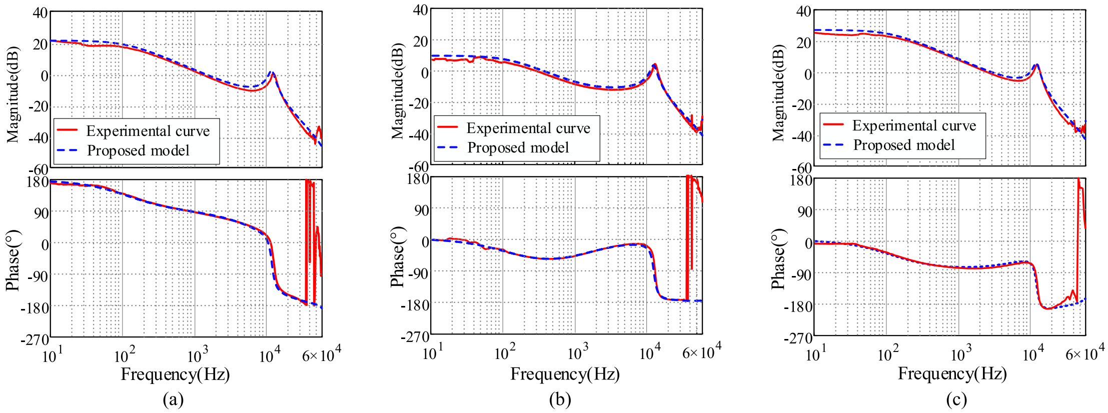

(a) (b) (c)

Fig. 28. Experimentally measured transfer functions of $G_{\mathrm{v}\varphi\_\mathrm{pri}}$ the DABSRC with primary-side regulation. (a) $\Phi = 0.3\pi$, (b) $\Phi = 0.5\pi$, (c) $\Phi = 0.7\pi$, respectively.

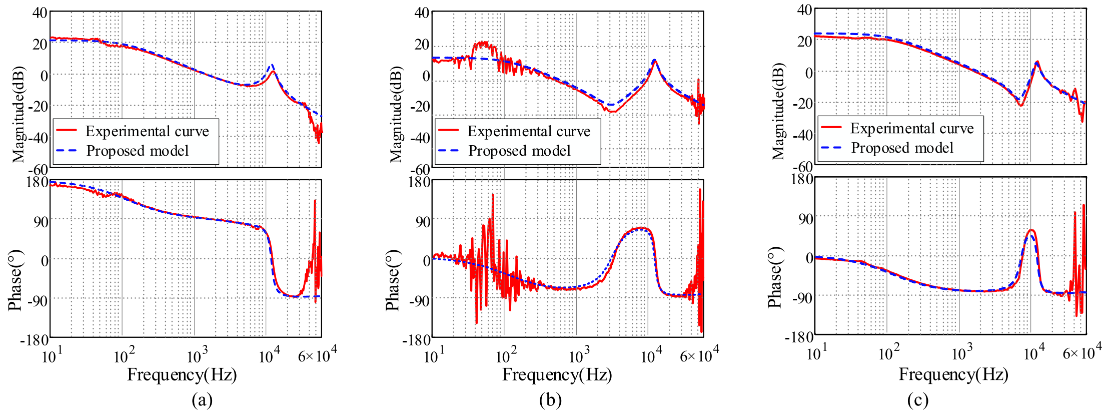

(a) (b) (c)

Fig. 29. Experimentally measured transfer functions of $G_{\mathrm{v}\varphi\_\mathrm{sec}}$ the DABSRC with secondary-side regulation. (a) $\Phi = 0.3\pi$, (b) $\Phi = 0.5\pi$, (c) $\Phi = 0.7\pi$, respectively.

rectifier bridge switches, causing calculated errors of $I_{\mathrm{s}}(T_{\varphi})$, which affects $G_{\mathrm{IR}}/\varphi(s)$ and finally leads to errors.

2) Effect of the Forward Voltage Drop of MOSFET's Antiparallel Diode: Forward voltage drop across MOSFETs' antiparallel diode is also not factored into the model. Fig. 24(c) and (d) show the simulation results for diode voltage drops of 0.7 V and 5 V, respectively. It can be seen that for $G_{\mathrm{v}\varphi\_\mathrm{pri}}$, the forward diode voltage drop has little effect and the simulation result overlaps with the proposed model curve across the entire frequency range. For $G_{\mathrm{v}\varphi\_\mathrm{sec}}$, the deviation of the model is small below 1/10 of the switching frequency, and is relatively large at higher frequencies. However, note that in the high frequency range, the amplitude and phase of $G_{\mathrm{v}\varphi\_\mathrm{sec}}$ changes so fast that the cut-off frequency will never be set in this range in practice. Therefore, this deviation does not affect the use of the model.

3) Effect of the Switching Frequency: Given that this article adopts the fundamental approximation, the proposed model achieves the highest accuracy when the switching frequency is close to the resonant frequency. Fig. 24(e) and (f) highlight the results when the switching frequency is far from the resonant frequency. It can be observed that the model accuracy is acceptable no matter when the switching frequency is below ($f_{\mathrm{n}} = 0.8$) or above ($f_{\mathrm{n}} = 3$) the resonant frequency. As DABSRC is usually designed in this frequency range, the proposed model is capable of meeting practical needs.

4) Effect of the Quality Factor: The quality factor Q value is an important parameter that characterizes the performance of DAB resonant converters. Here, the impact of Q on the proposed model is discussed by changing the load resistor R_{Ld} on the basis of the parameters in Table I. The Bode plots when Q value equal 0.1 and 10 are depicted here in Fig. 24(g) and (h). It can be seen that when the Q value is low, the proposed model exhibits very good accuracy. When Q increases to 10, a 2 dB error between $G_{\mathrm{v}\varphi\_\mathrm{sec}}$ and the simulation model in the high frequency range. This error is acceptable. Therefore, the proposed model has good adaptability to the change of Q.

V. EXPERIMENTAL VERIFICATION

A test platform composed of a DABSRC prototype, phase-shift controller and a vector network analyzer (VNA) Bode 100 is designed and built in the lab, as provided in Fig. 25. The circuit parameters are listed in Table I. The parameters of the DABSRC prototype closely match those outlined in Table I. Here, the load is configured to 73.8 Ω, and the switching frequency is adjusted to 60.3 kHz. The digital signal processor

(DSP) TMS320F280034 is employed to implement the phase shift schemes. The enhanced pulsewidth modulator (ePWM) modules of the DSP generate the driving signals, among which, ePWM1 is used to generate signals Q_1, Q_2 on the primary side, while ePWM2 is used to generate signals Q_3, Q_4 on the secondary side, which is consistent with Fig. 1.

Steady-state analysis is conducted first. three different steady-state phase-shift angle, $\Phi = 0.3\pi$ rad, $\Phi = 0.5\pi$ rad, and $\Phi = 0.7\pi$ rad are selected. Fig. 26 gives the time-domain operational waveforms, including the inverter-bridge voltage v_{AB}, the rectification voltage v_{CD}, the resonant current i_{AB}, and the output voltage v_{o}. Note that no matter using primary-side regulation or secondary-side regulation, the steady-state time-domain waveforms are exactly the same.

Transfer function measurement is the gold standard for validating models. The schematic diagram for measuring the transfer function $G_{\mathrm{v}\varphi}$ (s) is illustrated in Fig. 27. The measurement process initiates with Bode100 generating a sinusoidal sweep signal spanning frequencies from 100 Hz to 60 kHz. This signal undergoes galvanic isolation via a signal injection transformer, then is superimposed with offset voltage V_{dc1} or V_{dc2} to, respectively, modulate the comparator register values of ePWM1 or ePWM2 module after ADC conversion. In this way, the phase shift angle perturbation can be generated. After that, Q_1/Q_4 and Q_2/Q_3 are processed through parallel AND gates, with their respective outputs subsequently combined via an OR gate. The OR gate generates a rectangular wave with the pulsewidth proportional to the phase shift angle, and is transmitted to the Ref port of the VNA. The output voltage of the DAB resonant converter is sent to the Test port of VNA. The transfer function is the ratio of the Test port signal to the Ref port signal. The selection switches Q_{p} and Q_{s} determine the measurement mode of the transfer function, with Q_{p} specifically assigned to primary-side regulation and Q_{s} to secondary-side regulation.

The open-loop transfer function from the phase-shift angle to the output voltage, as derived in (39) and (54) are experimentally measured, which are, respectively, provided in Figs. 28 and 29, where we can see that they are consistent within half of the switching frequency range. Besides, comparing Figs. 28 and 29, it is also evident that the two models are indeed different. All of these have verified the correctness of the theoretical analysis.

VI. CONCLUSION

This article established a small-signal multifrequency model for DAB resonant converters with various resonant tanks. General control block diagram and the loop gain are obtained. The findings indicate that the model of the DAB resonant converter is contingent upon the particular manner in which its phase shifting is implemented; specifically, opting for primary-side regulation versus secondary-side regulation results in different zero distributions, and brings about distinct dynamic performance. Even if the same controller is used, the stability of the system will be different. Finally, A prototype of a DABSRC was built, and the accuracy of the proposed model was verified through transfer function measurements.

APPENDIX

This appendix gives the order reduction process of the DAB-SRC converter.

With regard to $G_{\mathrm{v}\varphi\_\mathrm{pri}}(j\omega_{\mathrm{p}})$, it can be mathematically manipulated into the following equivalent form (A1) shown at the bottom of this page.

It can be found that $G_{\mathrm{v}\varphi\_\mathrm{pri}}(j\omega_{\mathrm{p}})$ and $G_{\mathrm{v}\varphi\_\mathrm{sec}}(j\omega_{\mathrm{p}})$ are closely related to Z_{r} $[j(\omega_{\mathrm{p}}-\omega_{\mathrm{s}})]\cdot Z_{\mathrm{r}}[j(\omega_{\mathrm{p}}+\omega_{\mathrm{s}})]$, $Z_{\mathrm{r}}[j(\omega_{\mathrm{p}}-\omega_{\mathrm{s}})]+Z_{\mathrm{r}}[j(\omega_{\mathrm{p}}+\omega_{\mathrm{s}})]$ and Z_{r} $[j(\omega_{\mathrm{p}}+\omega_{\mathrm{s}})] - Z_{\mathrm{r}}[j(\omega_{\mathrm{p}}-\omega_{\mathrm{s}})]$, which will be simplified in sequence.

First, $Z_{\mathrm{r}}[j(\omega_{\mathrm{p}}-\omega_{\mathrm{s}})]\cdot Z_{\mathrm{r}}[j(\omega_{\mathrm{p}}+\omega_{\mathrm{s}})]$ can be solved to be

$$\begin{aligned} &Z_{\mathrm{r}}[j(\omega_{\mathrm{p}}-\omega_{\mathrm{s}})]Z_{\mathrm{r}}[j(\omega_{\mathrm{p}}+\omega_{\mathrm{s}})] \\ &= \left[j(\omega_{\mathrm{p}}-\omega_{\mathrm{s}})L_{\mathrm{r}} + \frac{1}{j(\omega_{\mathrm{p}}-\omega_{\mathrm{s}})C_{\mathrm{r}}} + R_{\mathrm{r}}\right] \\ &\quad \times \left[j(\omega_{\mathrm{p}}+\omega_{\mathrm{s}})L_{\mathrm{r}} + \frac{1}{j(\omega_{\mathrm{p}}+\omega_{\mathrm{s}})C_{\mathrm{r}}} + R_{\mathrm{r}}\right] \\ &= \frac{\omega_{\mathrm{p}}^2 L_{\mathrm{r}} C_{\mathrm{r}}\left(2+2\omega_{\mathrm{s}}^2 L_{\mathrm{r}} C_{\mathrm{r}} - \omega_{\mathrm{p}}^2 L_{\mathrm{r}} C_{\mathrm{r}}\right)}{(\omega_{\mathrm{p}}^2-\omega_{\mathrm{s}}^2)C_{\mathrm{r}}^2} \\ &\quad - \frac{\left(1-\omega_{\mathrm{s}}^2 L_{\mathrm{r}} C_{\mathrm{r}}\right)^2}{(\omega_{\mathrm{p}}^2-\omega_{\mathrm{s}}^2)C_{\mathrm{r}}^2} + j2\omega_{\mathrm{p}} R_{\mathrm{r}} L_{\mathrm{r}}\left(1+\frac{1}{\omega_{\mathrm{s}}^2 L_{\mathrm{r}} C_{\mathrm{r}}}\right) + R_{\mathrm{r}}^2. \end{aligned} \tag{A2}$$

When $\omega_{\mathrm{p}} << \omega_{\mathrm{s}}$, (A2) can be simplified as follows:

$$\begin{aligned} &Z_{\mathrm{r}}[j(\omega_{\mathrm{p}}-\omega_{\mathrm{s}})]Z_{\mathrm{r}}[j(\omega_{\mathrm{p}}+\omega_{\mathrm{s}})] \\ &\approx -2\omega_{\mathrm{p}}^2 L_{\mathrm{r}}^2\left(1+\frac{1}{\omega_{\mathrm{s}}^2 L_{\mathrm{r}} C_{\mathrm{r}}}\right) + \left(\omega_{\mathrm{s}} L_{\mathrm{r}} - \frac{1}{\omega_{\mathrm{s}} C_{\mathrm{r}}}\right)^2 \\ &\quad + {R_{\mathrm{r}}}^2 + j2\omega_{\mathrm{p}} R_{\mathrm{r}} L_{\mathrm{r}}\left[1+\frac{1}{\omega_{\mathrm{s}}^2 L_{\mathrm{r}} C_{\mathrm{r}}}\right]. \end{aligned} \tag{A3}$$

Defining

$$X_{\mathrm{eq}} = \omega_{\mathrm{s}} L_{\mathrm{r}} - \frac{1}{\omega_{\mathrm{s}} C_{\mathrm{r}}}, {Z_{\mathrm{eq}}}^2 = {X_{\mathrm{eq}}}^2 + {R_{\mathrm{r}}}^2, K_{\mathrm{eq}} = 1 + \frac{1}{\omega_{\mathrm{s}}^2 L_{\mathrm{r}} C_{\mathrm{r}}} \tag{A4}$$

(A3) becomes

$$\begin{aligned} &Z_{\mathrm{r}}[j(\omega_{\mathrm{p}}-\omega_{\mathrm{s}})]Z_{\mathrm{r}}[j(\omega_{\mathrm{p}}+\omega_{\mathrm{s}})] \\ &= -2\omega_{\mathrm{p}}^2 L_{\mathrm{r}}^2 K_{\mathrm{eq}} + {Z_{\mathrm{eq}}}^2 + j2\omega_{\mathrm{p}} R_{\mathrm{r}} L_{\mathrm{r}} K_{\mathrm{eq}}. \end{aligned} \tag{A5}$$

As for $Z_{\mathrm{r}}[j(\omega_{\mathrm{p}}-\omega_{\mathrm{s}})]+Z_{\mathrm{r}}[j(\omega_{\mathrm{p}}+\omega_{\mathrm{s}})]$, we have

$$Z_{\mathrm{r}}[j(\omega_{\mathrm{p}}-\omega_{\mathrm{s}})] + Z_{\mathrm{r}}[j(\omega_{\mathrm{p}}+\omega_{\mathrm{s}})]$$

$$G_{\mathrm{v}\varphi\_\mathrm{pri}}(j\omega_{\mathrm{p}}) = \frac{4V_{\mathrm{in}}Z_{\mathrm{RC}}(j\omega_{\mathrm{p}})}{j\pi^2}\cdot\frac{\cos(\Phi)\left(Z_{\mathrm{r}}[j(\omega_{\mathrm{p}}+\omega_{\mathrm{s}})] - Z_{\mathrm{r}}[j(\omega_{\mathrm{p}}-\omega_{\mathrm{s}})]\right) - j\sin(\Phi)\left(Z_{\mathrm{r}}[j(\omega_{\mathrm{p}}-\omega_{\mathrm{s}})] + Z_{\mathrm{r}}[j(\omega_{\mathrm{p}}+\omega_{\mathrm{s}})]\right)}{Z_{\mathrm{r}}[j(\omega_{\mathrm{p}}-\omega_{\mathrm{s}})]Z_{\mathrm{r}}[j(\omega_{\mathrm{p}}+\omega_{\mathrm{s}})] + \frac{4}{\pi^2}Z_{\mathrm{RC}}(j\omega_{\mathrm{p}})\left(Z_{\mathrm{r}}[j(\omega_{\mathrm{p}}-\omega_{\mathrm{s}})] + Z_{\mathrm{r}}[j(\omega_{\mathrm{p}}+\omega_{\mathrm{s}})]\right)} \tag{A1}$$

$$G_{\mathrm{v}\varphi\_\mathrm{pri}}(s)=\frac{V_{\mathrm{in}}R_{\mathrm{eq}}\left[-sL_{\mathrm{r}}K_{\mathrm{eq}}\sin\left(\Phi\right)+X_{\mathrm{eq}}\cos\left(\Phi\right)-R_{\mathrm{r}}\sin\left(\Phi\right)\right]}{\left(Z_{\mathrm{eq}}^{2}+2s^{2}L_{\mathrm{r}}^{2}K_{\mathrm{eq}}+2sR_{\mathrm{r}}L_{\mathrm{r}}+\frac{2sR_{\mathrm{r}}}{\omega_{\mathrm{s}}^{2}C_{\mathrm{r}}}\right)\left(1+sC_{\mathrm{o}}R_{\mathrm{Ld}}\right)+\left(sL_{\mathrm{r}}K_{\mathrm{eq}}+R_{\mathrm{r}}\right)R_{\mathrm{eq}}} \tag{A9}$$

$$G_{\mathrm{v}\varphi\_\mathrm{sec}}(s)=\frac{R_{\mathrm{eq}}}{Z_{\mathrm{eq}}}\cdot\frac{-\left[V_{\mathrm{in}}\sin\left(\Phi-\Theta_{\mathrm{Zr}}\right)+V_{\mathrm{o}}\sin\Theta_{\mathrm{Zr}}\right]\left(Z_{\mathrm{eq}}^{2}+2s^{2}L_{\mathrm{r}}^{2}K_{\mathrm{eq}}+2sR_{\mathrm{r}}L_{\mathrm{r}}+\frac{2sR_{\mathrm{r}}}{\omega_{\mathrm{s}}^{2}C_{\mathrm{r}}}\right)+Z_{\mathrm{eq}}V_{\mathrm{o}}X_{\mathrm{eq}}}{\left(Z_{\mathrm{eq}}^{2}+2s^{2}L_{\mathrm{r}}^{2}K_{\mathrm{eq}}+2sR_{\mathrm{r}}L_{\mathrm{r}}+\frac{2sR_{\mathrm{r}}}{\omega_{\mathrm{s}}^{2}C_{\mathrm{r}}}\right)\left(1+sC_{\mathrm{o}}R_{\mathrm{Ld}}\right)+\left(sL_{\mathrm{r}}K_{\mathrm{eq}}+R_{\mathrm{r}}\right)R_{\mathrm{eq}}} \tag{A12}$$

$$=j2\omega_{\mathrm{p}}L_{\mathrm{r}}+\frac{2\omega_{\mathrm{p}}}{j(\omega_{\mathrm{p}}^{2}-\omega_{\mathrm{s}}^{2})C_{\mathrm{r}}}+2R_{\mathrm{r}}. \tag{A6}$$

When $\omega_{\mathrm{p}} << \omega_{\mathrm{s}}$, (A6) can be simplified as follows:

$$Z_{\mathrm{r}}[j(\omega_{\mathrm{p}}-\omega_{\mathrm{s}})]+Z_{\mathrm{r}}[j(\omega_{\mathrm{p}}+\omega_{\mathrm{s}})]\approx j2\omega_{\mathrm{p}}L_{\mathrm{r}}K_{\mathrm{eq}}+2R_{\mathrm{r}}. \tag{A7}$$

Similarly, $Z_{\mathrm{r}}[j(\omega_{\mathrm{p}}+\omega_{\mathrm{s}})]-Z_{\mathrm{r}}[j(\omega_{\mathrm{p}}-\omega_{\mathrm{s}})]$ is simplified to be

$$Z_{\mathrm{r}}[j(\omega_{\mathrm{p}}+\omega_{\mathrm{s}})]-Z_{\mathrm{r}}[j(\omega_{\mathrm{p}}-\omega_{\mathrm{s}})]\approx j2X_{\mathrm{eq}}. \tag{A8}$$

Substitutions of (A5), (A7), and (A8) into (A1) lead to the following simplified expression of $G_{\mathrm{v}\varphi\_\mathrm{pri}}(s)$ (A9) shown at the top of this page.

Similar methodology can also be applied to $G_{\mathrm{v}\varphi\_\mathrm{sec}}(s)$. But the difference lies that the $I_{\mathrm{s}}(T_{\varphi})$ and the steady-state output voltage V_{o} should be deduced first. According to the FHA method, $I_{\mathrm{s}}(T_{\varphi})$ and V_{o} are solved as follows:

$$I_{\mathrm{s}}\left(T_{\varphi}\right)=\frac{4}{\pi}\mathrm{Im}\left[\frac{V_{\mathrm{in}}e^{j\Phi}-V_{\mathrm{o}}}{Z_{\mathrm{r}}\left(j\omega_{\mathrm{s}}\right)}\right] \tag{A10}$$

$$V_{\mathrm{o}}=V_{\mathrm{in}}\frac{R_{\mathrm{eq}}\cos\left(\Theta_{Zr}-\Phi\right)}{\left|Z_{r}\left(j\omega_{\mathrm{s}}\right)\right|+R_{\mathrm{eq}}\cos\left(\Theta_{Zr}\right)}. \tag{A11}$$

With (A10), (A11), the final expression of $G_{\mathrm{v}\varphi\_\mathrm{sec}}(s)$ is solved as follows after a tedious derivation (A12) shown at the top of this page.

REFERENCES

[1] X. Li and A. K. S. Bhat, "Analysis and design of high-frequency isolated dual-bridge series resonant DC/DC converter," *IEEE Trans. Power Electron.*, vol. 25, no. 4, pp. 850–862, Apr. 2010, doi: 10.1109/TPEL.2009.2034662.

[2] Y. Wu, C. Liu, M. Zhou, X. Mao, and Y. Zhang, "An anti-offset electric vehicle wireless charging system based on dual coupled antiparallel coils," *IEEE Trans. Power Electron.*, vol. 38, no. 5, pp. 5634–5637, May 2023.

[3] H. Tang et al., "A self-adaptive dual-channel LCC-S detuned topology for misalignment tolerance in AUV wireless power transfer systems," *IEEE Trans. Power Electron.*, vol. 40, no. 3, pp. 4630–4639, Mar. 2025, doi: 10.1109/TPEL.2024.3492194.

[4] G. Pavlov, A. Obrubov, and I. Vinnichenko, "The linearized dynamic model of the series resonant converter for small signals," in *Proc. Int. Conf. Intell. Energy Power Syst.*, 2016, pp. 1–5.

[5] P. Zumel, L. D. Ortega, C. Fernandez, R. Rodriguez, and A. Barrado, "Discrete model of dual active bridge series resonant converter," in *Proc. 20th Workshop Control ModelPower Electron.*, Jun. 2019, pp. 1–7.

[6] F. Ibanez, J. M. Echeverria, J. Vadillo, and L. Fontan, "Frequency response analysis for bidirectional series resonant DC/DC converter in discontinuous mode," *IET Power Electron.*, vol. 7, no. 9, pp. 2374–2386, 2014.

[7] Y. Pan, Y. Yang, J. He, A. Sangwongwanich, and F. Blaabjerg, "Low-frequency oscillation suppression in series resonant dual-active-bridge converters under fault tolerant operation," in *Proc. 2019 IEEE Energy Convers. Congr. Expo.*, 2019, pp. 1499–1505.

[8] Y. Pan et al., "A dual-loop control to ensure fast and stable fault-tolerant operation of series resonant dab converters," *IEEE Trans. Power Electron.*, vol. 35, no. 10, pp. 10994–11012, Oct. 2020.

[9] W. Song, M. Zhong, S. Luo, and S. Yang, "Model predictive power control for bidirectional series-resonant isolated DC–DC converters with fast dynamic response in locomotive traction system," *IEEE Trans. Transp. Electrific.*, vol. 6, no. 3, pp. 1326–1337, Sep. 2020.

[10] A. K. Dubey and N. Lakshminarasamma, "Modeling of series resonant dual active bridge converter for dc microgrid application," in *Proc. 2022 IEEE Int. Conf. Environ. Elect. Eng. 2022 IEEE Ind. Commercial Power Syst. Europe*, 2022, pp. 1–6.

[11] D. Seltzer, L. Corradini, D. Bloomquist, R. Zane, and D. Maksimović, "Small signal phasor model. dual act. bridge ser. resonant dc/dc converters with multi-angle phase shift modulation," in *Proc 2011 IEEE Energy Convers. Congr. Expo.*, 2011, pp. 2757–2764.

[12] D. Seltzer, D. Bloomquist, R. Zane, and D. Maksimovic, "Gain-scheduled control of multi angle phase shift modulated dual active bridge series resonant DC/DC converters," in *Proc. 2012 IEEE 13th Workshop Control Model. Power Electron.*, 2012, pp. 1–7.

[13] S. M. Tayebi, S. Rajendran, A. Sun, and A. Q. Huang, "Generalized average modeling of a single-stage resonant-based inverter," in *Proc. 2020 IEEE Appl. Power Electron. Conf. Expo.*, 2020, pp. 3068–3073.

[14] W. L. Malan, D. M. Vilathgamuwa, and G. R. Walker, "Modeling and control of a resonant dual active bridge with a tuned CLLC network," *IEEE Trans. Power Electron.*, vol. 31, no. 10, pp. 7297–7310, Oct. 2016.

[15] Z. Gao, C. Jin, K. Liu, and J. Zhao, "Analysis and modeling of multimode operation for series-parallel CLLC resonant converter," in *Proc. 2020 IEEE Power Energy Conf. Illinois*, 2020, pp. 1–6.

[16] W. L. Malan, D. M. Vilathgamuwa, G. Walker, D. J. Thrimawithana, and U. K. Madawala, "Modeling and control of a CLC resonant dual active bridge," in *Proc. Australas. Universities Power Eng. Conf.*, 2014, pp. 1–6.

[17] K. Li et al., "Modeling and hybrid controller design of CLLLC," in *Proc. 2019 IEEE 10th Int. Symp. Power Electron. Distrib. Gener. Syst.*, 2019, pp. 168–172.

[18] L. Scandola, L. Corradini, and G. Spiazzi, "Small-signal modeling of combined phase shift and pulse width uniformly sampled modulators," in *Proc. 2015 IEEE 16th Workshop Control Model. Power Electron.*, 2015, pp. 1–7.

[19] Y. Qiu, M. Xu, K. Yao, J. J. Sun, and F. C. Lee, "Multifrequency small-signal model for buck and multiphase interleaving buck converters," *IEEE Trans. Power Electron.*, vol. 21, no.no. 5, pp. 1185–1192, Sep. 2006.

[20] X. Li, Y. Zhang, S. Chen, X. Zhang, and Y. Tang, "General multi-frequency small-signal model for resonant converters," *IEEE Trans. Power Electron.*, vol. 37, no. 4, pp. 3892–3912, Apr. 2022.